

# Mantis: Mamba-native Tuning is Efficient for 3D Point Cloud Foundation Models

Zihao Guo<sup>1</sup> Jihua Zhu<sup>1\*</sup> Jian Liu<sup>2</sup> Ajmal Saeed Mian<sup>3</sup>

<sup>1</sup>Xi'an Jiaotong University, Xi'an, China

<sup>2</sup>Singapore University of Technology and Design, Singapore

<sup>3</sup>University of Western Australia, Perth, Australia

Gzhao924@163.com

## Abstract

Pre-trained 3D point cloud foundation models (PFMs) have demonstrated strong transferability across diverse downstream tasks. However, full fine-tuning these models is computationally expensive and storage-intensive. Parameter-efficient fine-tuning (PEFT) offers a promising alternative, but existing PEFT approaches are primarily designed for Transformer-based backbones and rely on token-level prompting or feature transformation. Mamba-based backbones introduce a granularity mismatch between token-level adaptation and state-level sequence dynamics. Consequently, straightforward transfer of existing PEFT approaches to frozen Mamba backbones leads to substantial accuracy degradation and unstable optimization. To address this issue, we propose Mantis, the first Mamba-native PEFT framework for 3D PFMs. Specifically, a State-Aware Adapter (SAA) is introduced to inject lightweight task-conditioned control signals into selective state-space updates, enabling state-level adaptation while keeping the pre-trained backbone frozen. Moreover, different valid point cloud serializations are regularized by Dual-Serialization Consistency Distillation (DSCD), thereby reducing serialization-induced instability. Extensive experiments across multiple benchmarks demonstrate that our Mantis achieves competitive performance with only about 5% trainable parameters. Our code is available at <https://github.com/gzhhhhhh/Mantis>.

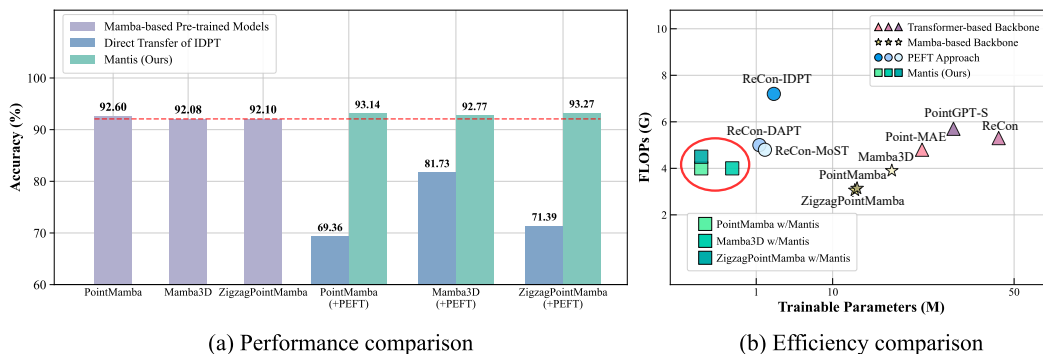


Figure 1: Comprehensive comparisons between our Mantis and several representative counterparts[4, 30, 27, 12, 23, 7, 48, 57, 13] on OBJ\_ONLY variant of ScanObjectNN dataset[36]. (a) Our Mantis achieves superior performance over existing counterparts. (b) Our Mantis achieves an ideal trade-off between trainable parameters and FLOPs (G).

\*Corresponding author.

# 1 Introduction

Fine-tuning pre-trained point cloud foundation models (PFMs) has been demonstrated to adapt effectively to diverse downstream tasks[47, 27, 53, 4, 49]. However, the computational and storage costs associated with full fine-tuning are prohibitively high, particularly as model sizes continue to grow[15, 16, 35, 57, 4, 30]. To alleviate this burden, parameter-efficient fine-tuning (PEFT) methods[40, 24, 50, 13, 57], such as Instance-aware Dynamic Prompt Tuning (IDPT)[48], have emerged as promising alternatives, garnering significant attention. Instead of updating all model parameters directly, IDPT applies DGCNN[42] to extract dynamic prompts for different instances. This approach significantly reduces the number of parameters that need to be fine-tuned, thereby lowering the computational and memory overhead.

Follow-up research in 3D point cloud analysis can be roughly categorized into Prompt Tuning[48, 1], Adapters[57, 51, 50, 35, 24] and Reparameterization[13, 40]. Despite these advancements, most of the prior art still relies on Transformer-native architectures[47, 27, 53, 4]. However, Transformer-based models incur quadratic token-length complexity and significant resource overhead, especially for large-scale point clouds and fine-grained tokenization. In parallel, recent advances in State Space Models (SSMs), particularly Mamba, offer a linear-time alternative to Transformer-based modeling[10, 9]. This advantage has already motivated a growing body of work on Mamba-based point cloud backbones, including PointMamba[23] and related variants [12, 55, 7, 55].

Unfortunately, to the best of our knowledge, there is still no dedicated Mamba-native PEFT framework designed for 3D point cloud backbones. More critically, directly transferring existing PEFT approaches to frozen Mamba-based backbones leads to substantial accuracy degradation and severe optimization instability, as illustrated in Figure 1 (a). The catastrophic performance drop can be attributed to two fundamental mismatches. First, Transformer-native PEFT approaches operate at the token level, whereas Mamba models rely on state-level sequence dynamics, resulting in a granularity mismatch with frozen Mamba backbones. Second, point cloud Mamba models are sensitive to serialization-dependent state propagation, which is an inherent gap in the order-agnostic PEFT modules. This implies that indiscriminately applying existing PEFT approaches may undermine the potential of the Mamba architecture. This motivates the need for a Mamba-native PEFT framework.

In this paper, we propose Mantis, the first Mamba-native adaptation framework with two complementary components. State-Aware Adapter (SAA) integrates task-conditioned control signals into the Mamba state-space updates, bypassing token-level prompts and addressing the inherent granularity mismatch, while Dual-Serialization Consistency Distillation (DSCD) enforces consistent representations across two valid serializations of the same point cloud, regularizing order-sensitive state propagation and improving the preservation of pretrained geometric priors.

With the proposed components, our Mantis achieves better performance than full fine-tuning, while utilizing only about 5% of the trainable parameters. Especially, Mantis with 0.8M parameters achieves 93.29%, 92.77%, and 93.48% in the three ScanObjectNN[36] variants on Mamba3D[12], surpassing the full fine-tuning with 16.9M parameters by + **0.17%**, + **0.69%** and + **1.43%**, respectively. Notably, by optimizing only lightweight task-specific modules, Mantis substantially reduces the trainable parameters and storage cost for downstream tasks, while preserving Mamba’s linear-complexity modeling paradigm, as illustrated in Figure 1 (b).

The main contributions of this work are summarized as follows:

- We reveal a fundamental gap between Transformer-native PEFT methods and Mamba-based backbones. To fill this gap, we propose Mantis, the first Mamba-native parameter-efficient fine-tuning framework for 3D point cloud analysis.
- Building upon our insights into the granularity mismatch, we propose **State-Aware Adapter (SAA)**, which injects task-conditioned control signals into Mamba state updates.
- Derived from the serialization-sensitive nature of Mamba modeling, we introduce **Dual-Serialization Consistency Distillation (DSCD)** for cross-serialization consistency and stable downstream optimization.
- Extensive experiments demonstrate the effectiveness and efficiency of our approach, shedding light on Mamba-native PEFT for future research.

## 2 Related work

### 2.1 Point cloud foundation models

PFMs are pre-trained on a pretext task, followed by fine-tuning for downstream applications. Architecturally, existing 3D PFMs can be divided into Transformer-based[4, 27, 49, 56, 43, 44] and Mamba-based[23, 12, 7, 55] categories. Initially proposed for natural language processing[38, 6], Transformer-based approaches leverage self-attention to capture long-range dependencies and global context in 3D point cloud analysis. For instance, PointBERT[47], PointMAE[27] and PointM2AE[53] simplify pre-training via masked autoencoding. Multimodal integration further enriches learned representations. ReCon[30] and HyperPoint[33] embed contrastive objectives into generative pipelines to avoid overfitting in Transformer-based approaches.

Meanwhile, Mamba-based approaches have emerged as a new paradigm for PFMs, offering efficient alternatives to Transformers by relying on SSMs. PointMamba[23] pioneers point cloud modeling, providing strong global representations for downstream tasks, while Mamba3D[12] focuses on enhancing local features. HydraMamba[31], StruMamba3D[39] and OctMamba[18] employ various space-filling curves to form causal sequences for SSM. In contrast to the above methods, PCM[55] and CloudMamba[32] directly build structural dependencies without explicit curve parameterization. While these pre-trained 3D vision models with full fine-tuning have demonstrated exceptional capabilities for various downstream 3D tasks, the high computational costs and potential dilution of pre-trained knowledge motivate our exploration of efficient fine-tuning strategies.

### 2.2 Parameter-efficient fine-tuning

As highlighted above, PFMs are iterating at an unprecedented pace in terms of structure[34], method[41, 20], and applications[52]. This momentum has rendered the PEFT community equally dynamic. PEFT in 3D point cloud approaches mainly fall into prompt-based[48, 1], adapter-based[57, 51, 50, 35, 24] and reparameterization-based[13, 40]. Prompt-based approaches add learnable tokens to input data or attention layers to guide task-specific tuning. For example, IDPT[48] introduces instance-aware dynamic prompts to improve robustness during downstream adaptation. Meanwhile, adapter-based pioneers like DAPT[57] combines dynamic adapter scaling with prompt generation to better match downstream token significance. In order to overcome the limitation in inference overhead, reparameterization-based approaches reformulate the network weights, enabling parameter-efficient adaptation. PointLoRA[40] brings low-rank adaptation with local token priors to fine-tuning and MoST[13] brings Monarch-based sparse reparameterization with local geometric priors. However, these tuning approaches are specifically designed for Transformer-based backbones, which limits their adaptability to Mamba-based models. In contrast, our Mantis, the first Mamba-native parameter-efficient fine-tuning framework for 3D point cloud analysis, fills the underexplored gap in PEFT for Mamba-based backbones and enables efficient adaptation to downstream tasks while preserving Mamba’s linear-complexity modeling.

## 3 Methods

### 3.1 Preliminaries: State Space Models and PointMamba

Drawing inspiration from control theory, State Space Models (SSMs) map an input sequence  $x_t$  to an output  $y_t$  through a latent state  $h_t$ . In its discretized form, the transformation can be written as:

$$h_t = \bar{A}h_{t-1} + \bar{B}x_t, \quad y_t = Ch_t, \quad (1)$$

where  $\bar{A}$  and  $\bar{B}$  are the discretized state transition and input projection matrices. While early structured SSMs rely on fixed transition parameters, Mamba (S6)[9] introduces input-dependent parameters  $(B, C, \Delta)$ , enabling selective and content-aware sequence modeling.

For point cloud analysis, PointMamba[23] adopts the SSM framework by treating serialized point tokens as sequential inputs. The state update can be written as:

$$h_t = \bar{A}_t h_{t-1} + \bar{B}_t x_t, \quad y_t = C_t h_t, \quad (2)$$

where  $h_t$  denotes the hidden state,  $x_t$  denotes the input point token, and  $\bar{A}_t$ ,  $\bar{B}_t$ , and  $C_t$  are input-dependent operators. This selective state update provides efficient sequence modeling, but also causes the hidden-state propagation to depend on the serialized point order.

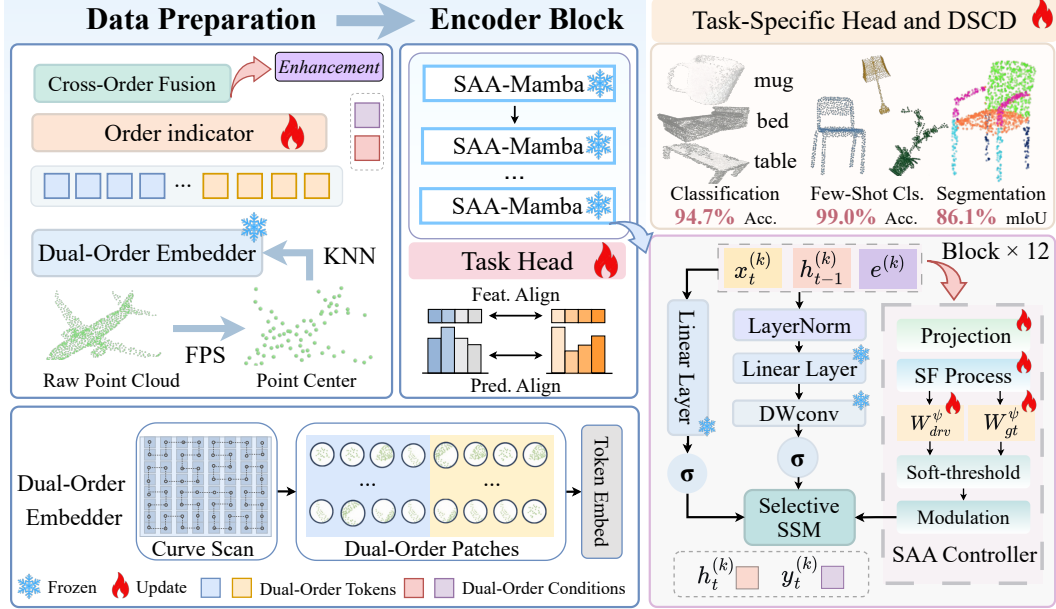


Figure 2: **Pipeline of Mantis.** Raw point clouds are sampled using Farthest Point Sampling (FPS) to select representative key points, and local neighborhoods are formed via K-nearest neighbors (KNN) for each key point. The resulting patches are serialized along two complementary space-filling curves to produce dual-order patches. These patches are fused and processed by stacked SAA-Mamba blocks, where the selective SSM is modulated by the SAA controller. DSCD regularizes cross-serialization consistency at both feature and prediction levels during training. Task-specific heads perform classification, few-shot learning, or part segmentation. During training, the backbone is frozen and only newly added parameters are fine-tuned.  $\sigma$  indicates SiLU activation.

### 3.2 Overall pipeline

The pipeline of our approach is shown in Figure 2. Given an input point cloud  $P \in \mathbb{R}^{M \times 3}$ , we first utilize FPS to sample  $n$  key points, denoted as  $p \in \mathbb{R}^{n \times 3}$ . The order of key points  $p$  is generally random, which does not affect previous Transformer-based approaches due to their inherent order-invariance. However, for the selective SSM, its unidirectional modeling struggles with unstructured point clouds. To address this, building on the pioneer works[23], we leverage space-filling curves (e.g., the Hilbert curve[14] and its transposed variant) for dual-order serialization, transforming the unstructured point clouds into regular sequences, denoted as  $p_h$  and  $p_{h'}$ . We then apply the KNN algorithm to select  $K$  nearest neighbors for each key point, forming  $n$  token patches  $\mathcal{N}_h^{(1)} \in \mathbb{R}^{n \times K \times 3}$  and  $\mathcal{N}_{h'}^{(2)} \in \mathbb{R}^{n \times K \times 3}$  with patch size  $K$ . To map the local patches to feature space, we employ a lightweight PointNet[28] to obtain serialized point tokens  $E_h^{(1)} \in \mathbb{R}^{n \times d}$  and  $E_{h'}^{(2)} \in \mathbb{R}^{n \times d}$ .

Different from existing approaches that employ feature-wise affine transformations as order indicators[23], we model the serialization order as a conditioning signal that modulates the representation in a residual manner. Specifically, for each branch  $k \in \{1, 2\}$ , we introduce a learnable order embedding  $o^{(k)} \in \mathbb{R}^{d_o}$ . The order-aware representation  $e^{(k)} \in \mathbb{R}^d$  is formulated as follows:

$$e^{(k)} = \text{MaxPool}(E^{(k)} + \mathcal{G}(E^{(k)}) \odot \varphi(o^{(k)})), \quad (3)$$

where  $\mathcal{G}(\cdot)$  denotes a lightweight transformation on the input features, and  $\varphi(\cdot)$  maps the order embedding to a modulation vector in the feature space.  $\odot$  denotes element-wise product. The two serialized sequences capture complementary structural cues under different traversal orders. We employ a lightweight channel-wise fusion to bridge the two orders, while DSCD enforces cross-order consistency during training. The fused representations  $Z_0^{(k)} \in \mathbb{R}^{n \times d}$  are then fed into a non-hierarchical encoder composed of stacked SAA-Mamba blocks. Each SAA-Mamba block follows the general design of a Mamba layer, consisting of layer normalization, linear projection, depth-wise convolution, selective state-space modeling, and residual connection. Specifically, given

the input  $Z_{l-1}^{(k)}$  to the  $l$ -th block, we first obtain the intermediate features by:

$$\tilde{Z}_l^{(k)} = \text{Linear}\left(\text{LayerNorm}(Z_{l-1}^{(k)})\right), \quad X_l^{(k)} = \sigma\left(\text{DWConv}\left(\tilde{Z}_l^{(k)}\right)\right), \quad (4)$$

where  $\sigma$  indicates SiLU activation. The resulting feature matrix  $X_l^{(k)}$  is then fed into the selective SSM for sequence modeling. Different from standard Mamba blocks, we introduce a **State-Aware Adapter (SAA)** controller to modulate the state transition dynamics within the selective SSM. The output of the  $l$ -th block is computed as:

$$Z_l^{(k)} = \mathcal{F}_{\text{SAA}}\left(X_l^{(k)}\right) + \sigma\left(\text{Linear}(Z_{l-1}^{(k)})\right), \quad (5)$$

where  $\mathcal{F}_{\text{SAA}}(\cdot)$  denotes the selective SSM enhanced with the proposed State-Aware Adapter.

### 3.3 State-Aware Adapter

In the SAA-Mamba block described above, the State-Aware Adapter modulates the selective state-space dynamics by acting on the state transition operators. Specifically, the state update is governed by  $\mathbf{A}_t$ ,  $\mathbf{B}_t$ ,  $\mathbf{C}_t$ , which define the write, propagation, and read processes of the hidden state. Based on this observation, we introduce a lightweight, task-conditioned control signal to modulate these operators, enabling input-dependent adaptation of the state evolution. In contrast to LoRA-style static weight updates[16], our control signal is input-dependent and dynamically modulates the state evolution at each step. Moreover, SAA operates at the state level rather than token or feature-level representations, providing fine-grained control over sequence dynamics while keeping the backbone frozen. At each sequence step  $t$ , the SAA controller takes the current token  $x_t^{(k)}$ , the previous hidden state  $h_{t-1}^{(k)}$ , and the order-aware representation  $e^{(k)}$  as inputs. These signals are first projected into a shared control space and then encoded as:

$$\phi_t^{(k)} = \Phi\left(W_x^\phi x_t^{(k)} \parallel W_h^\phi h_{t-1}^{(k)} \parallel W_e^\phi e^{(k)}\right), \quad (6)$$

where  $\Phi(\cdot)$  denotes the state fusion process,  $\parallel$  denotes feature-wise concatenation,  $W_x^\phi \in \mathbb{R}^{d_\phi \times d}$ ,  $W_h^\phi \in \mathbb{R}^{d_\phi \times d_n}$ , and  $W_e^\phi \in \mathbb{R}^{d_\phi \times d}$  are learnable projection matrices that map the token, hidden state, and order-aware representation into a shared  $d_\phi$ -dimensional control space, respectively. We formulate control signal generation as a proximal optimization problem, which admits a closed-form soft-thresholding solution. Specifically, denote  $\mathbf{q}_t^{(k)} = W_{\text{drv}}^\psi \phi_t^{(k)}$ , and  $\lambda_t^{(k)} = -\log \sigma\left(W_{\text{gt}}^\psi \phi_t^{(k)}\right)$ . The optimal sparse control signal is obtained by minimizing:

$$\mathbf{u}_t^{(k)} = \arg \min_{\mathbf{v}} \frac{1}{2} \left\| \mathbf{q}_t^{(k)} - \mathbf{v} \right\|_2^2 + \sum_i \lambda_{t,i}^{(k)} |v_i|, \quad (7)$$

where  $v_i$  is the  $i$ -th entry of the optimization variable  $\mathbf{v} \in \mathbb{R}^r$ . Its closed-form solution is the component-wise thresholding operator:

$$u_{t,i}^{(k)} = \begin{cases} q_{t,i}^{(k)} - \lambda_{t,i}^{(k)}, & \text{if } q_{t,i}^{(k)} > \lambda_{t,i}^{(k)}, \\ 0, & \text{if } |q_{t,i}^{(k)}| \leq \lambda_{t,i}^{(k)}, \\ q_{t,i}^{(k)} + \lambda_{t,i}^{(k)}, & \text{if } q_{t,i}^{(k)} < -\lambda_{t,i}^{(k)}, \end{cases} \quad (8)$$

where  $q_{t,i}^{(k)}$  and  $\lambda_{t,i}^{(k)}$  denote the  $i$ -th element of  $\mathbf{q}_t^{(k)}$  and  $\lambda_t^{(k)}$ , respectively.  $W_{\text{drv}}^\psi, W_{\text{gt}}^\psi \in \mathbb{R}^{r \times d_\phi}$  are learnable projection matrices, and  $r \ll d$  denotes the bottleneck dimension. To achieve task-conditioned adaptation, we propose to directly modulate the state transition operators  $(\mathbf{A}_t^{(k)}, \mathbf{B}_t^{(k)}, \mathbf{C}_t^{(k)}, \mathbf{\Delta}_t^{(k)})$  via the control signal  $\mathbf{u}_t^{(k)}$ ,

$$\begin{bmatrix} \tilde{\mathbf{A}}_t^{(k)} & \tilde{\mathbf{B}}_t^{(k)} & \tilde{\mathbf{C}}_t^{(k)} & \tilde{\mathbf{\Delta}}_t^{(k)} \end{bmatrix}^T = \begin{bmatrix} \mathbf{A}_t^{(k)} & \mathbf{B}_t^{(k)} & \mathbf{C}_t^{(k)} & \mathbf{\Delta}_t^{(k)} \end{bmatrix}^T + \mathbf{U} \text{diag}(\mathbf{u}_t^{(k)}) \mathbf{V}, \quad (9)$$

where  $\mathbf{U} \in \mathbb{R}^{m \times r}$  and  $\mathbf{V} \in \mathbb{R}^{r \times m}$  are low-rank modulation matrices, and  $\text{diag}(\mathbf{u}_t^{(k)})$  encodes the task-conditioned sparse control signal, which modulates all operators  $(\mathbf{A}_t, \mathbf{B}_t, \mathbf{C}_t, \mathbf{\Delta}_t)$ . This unified

modulation enables fine-grained operator adaptation with minimal overhead. The controlled operators are then discretized via zero-order hold (ZOH) to yield the discrete-time system:

$$\widehat{\mathbf{A}}_t^{(k)} = \exp\left(\widetilde{\mathbf{A}}_t^{(k)} \widetilde{\Delta}_t^{(k)}\right), \quad \widehat{\mathbf{B}}_t^{(k)} = \left(\widetilde{\mathbf{A}}_t^{(k)}\right)^{-1} \left(\exp\left(\widetilde{\mathbf{A}}_t^{(k)} \widetilde{\Delta}_t^{(k)}\right) - \mathbf{I}\right) \widetilde{\mathbf{B}}_t^{(k)}, \quad (10)$$

where  $\widetilde{\Delta}_t^{(k)}$  controls the temporal discretization, and  $\mathbf{I}$  denotes the identity matrix with a compatible dimension. The output of the dynamical system is given by:

$$h_t^{(k)} = \widehat{\mathbf{A}}_t^{(k)} h_{t-1}^{(k)} + \widehat{\mathbf{B}}_t^{(k)} x_t^{(k)}, \quad y_t^{(k)} = \widetilde{\mathbf{C}}_t^{(k)} h_t^{(k)}. \quad (11)$$

As a consequence, the proposed State-Aware Adapter formulates the selective SSM as a conditionally controlled dynamical system, enabling direct modulation of state evolution. Appendix A.2 further analyzes how SAA modifies the selective transfer kernel through sparse low-rank perturbations and explains its stability by bounding the hidden-state deviation under bounded operator perturbations.

### 3.4 Dual-Serialization Consistency Distillation

Although serialization enables Mamba to process unordered point clouds as sequential inputs, the resulting hidden-state propagation is inherently sensitive to the specific traversal order. Consequently, different valid serializations of the same point cloud may induce inconsistent feature representations and unstable predictions, which hinders reliable adaptation under frozen Mamba backbones. We provide a transfer-kernel analysis of this serialization sensitivity in Appendix A.1.

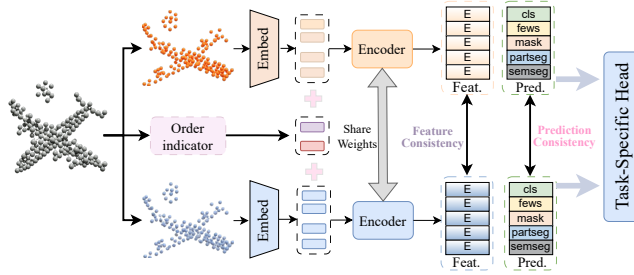


Figure 3: **Illustration of Dual-Serialization Consistency Distillation.** During training, DSCD enforces cross-serialization consistency at both feature and prediction levels.

To alleviate this issue, we propose **Dual-Serialization Consistency Distillation (DSCD)**, which enforces cross-order consistency by aligning feature representations and predictive distributions across two serialization views, as illustrated in Figure 3. Built upon the dual-serialization pipeline described above, DSCD regularizes the two serialization branches at the final encoder layer. The final-layer output of branch  $k$  is denoted by  $Z_L^{(k)}$ , and the feature alignment loss is formulated as:

$$z^{(k)} = g_\varphi\left(\text{AvgPool}(Z_L^{(k)})\right), \quad \mathcal{L}_{\text{feat}} = \left\| \frac{z^{(1)}}{\|z^{(1)}\|_2} - \frac{z^{(2)}}{\|z^{(2)}\|_2} \right\|_2^2, \quad (12)$$

where  $g_\varphi$  is a branch-shared projection mapping. While  $\mathcal{L}_{\text{feat}}$  enforces representation-level consistency across different serialization orders, stable downstream optimization further requires alignment at the decision level. The prediction-level consistency term is defined as:

$$\pi^{(k)} = \text{Softmax}\left(\ell^{(k)}/\tau\right), \quad \mathcal{L}_{\text{pred}} = \frac{1}{2} \text{KL}\left(\pi^{(1)} \parallel \pi^{(2)}\right) + \frac{1}{2} \text{KL}\left(\pi^{(2)} \parallel \pi^{(1)}\right), \quad (13)$$

where  $\tau$  is the temperature hyperparameter, and  $\pi^{(k)}$  denotes the softened predictive distribution of branch  $k$ . Accordingly, the training objective can be defined as follows:

$$\mathcal{L} = \mathcal{L}_{\text{task}} + \alpha \mathcal{L}_{\text{feat}} + \beta \mathcal{L}_{\text{pred}}, \quad (14)$$

where  $\alpha$  and  $\beta$  are coefficients for feature consistency and prediction consistency, respectively. By reducing cross-serialization discrepancies at both the representation and prediction levels, DSCD improves cross-serialization consistency and stabilizes downstream optimization.

## 4 Experiments

We evaluate Mantis on multiple downstream tasks, including object classification, part segmentation, and few-shot learning. We utilize three pre-trained models (PointMamba[23], Mamba3D[12], and ZigzagPointMamba[7]) as our baselines. For a fair comparison, we follow the default fine-tuning settings of each baseline. The hyperparameters are set as  $\alpha = 100$ ,  $\beta = 0.05$ , and  $\tau = 1$ . Additional analyses of  $\alpha$  and  $\beta$  and training details can be found in the Appendix B.

Table 1: Classification on three variants of ScanObjectNN[36] and ModelNet40[45], including the number of trainable parameters, FLOPs and overall accuracy (OA). #TP (M) represents the trainable parameters. Attn. denotes attention-based (Transformer) and SSM denotes state-space model (Mamba). † indicates that using simple rotational augmentation[8] for training. ◦ and ○ denote methods that leverage cross-modal and single-modal information, respectively. ModelNet40 results report the overall accuracy from 1024 points without voting. \* denotes results reproduced from the public source code. The best two results are bolded and underlined respectively. Same as follows.

Methods	Reference	Backbone	#TP (M)↓	FLOPs (G)	ScanObjectNN↑			ModelNet40↑
					OBJ_BG	OBJ_ONLY	PB_T50_RS	OA (%)
<i>Supervised Learning Only</i>								
◦ PointNet[28]	CVPR17	-	3.5	0.5	73.3	79.2	68.0	89.2
◦ PointNet++[29]	NeurIPS17	-	1.5	1.7	82.3	84.3	77.9	90.7
◦ PointCNN[22]	NeurIPS18	-	0.6	0.9	86.1	85.5	78.5	92.2
◦ DGCNN[42]	TOG19	-	1.8	2.4	82.8	86.2	78.1	92.9
<i>Self-Supervised Learning (Full Fine-tuning)</i>								
◦ Point-BERT[47]	CVPR22	Attn.	22.1	4.8	87.43	88.12	83.07	93.2
◦ Point-M2AE[53]	NeurIPS22	Attn.	15.3	3.6	91.22	88.81	86.43	94.0
◦ PointGPT-S†[4]	NeurIPS23	Attn.	29.2	5.7	93.39	92.43	89.17	93.3
◦ ACT†[8]	ICLR23	Attn.	22.1	4.8	93.29	91.91	88.21	93.6
◦ Joint-MAE[11]	IJCAI23	Attn.	-	-	90.94	88.86	86.07	94.0
◦ I2P-MAE†[54]	CVPR23	Attn.	15.3	-	94.15	91.57	90.11	93.4
◦ PCM[55]	AAAI25	SSM	34.2	-	-	-	88.10	93.4
◦ SI-Mamba[3]	CVPR25	SSM	12.3	3.6	92.25	91.39	87.30	92.7
<i>Self-Supervised Learning (Parameter-Efficient Fine-Tuning)</i>								
◦ Point-MAE[27]	ECCV22	Attn.	22.1 (100%)	4.8	90.02	88.29	85.18	93.8
+ IDPT[48]	ICCV23	Attn.	1.7 (7.7%)	7.2	91.22 (+ 1.20)	90.02 (+ 1.73)	84.94 (- 0.24)	93.3 (- 0.5)
+ PointLoRA[40]	CVPR25	Attn.	0.8 (3.6%)	-	90.71 (+ 0.69)	89.33 (+ 1.04)	85.53 (+ 0.35)	93.3 (- 0.5)
◦ ReCon†[30]	ICML23	Attn.	43.6 (100%)	5.3	<b>95.18</b>	<b>93.63</b>	90.63	<u>94.1</u>
+ DAPT[57]	CVPR24	Attn.	1.1 (2.5%)	5.0	94.32 (- 0.86)	92.43 (- 1.20)	89.38 (- 1.25)	93.5 (- 0.6)
+ GAPrompt[1]	ICML25	Attn.	0.6 (1.4%)	5.0	94.49 (- 0.69)	92.60 (- 1.03)	89.76 (- 0.87)	94.0 (- 0.1)
◦ PointMamba†[23]	NeurIPS24	SSM	12.3 (100%)	3.1	94.32	92.60	89.31	93.6
+ PMA†[50]	CVPR25	SSM	1.1 (8.9%)	5.2	93.53 (- 0.79)	91.32 (- 1.28)	86.71 (- 2.60)	93.6 (+ 0.0)
+ Mantis†	<b>This Paper</b>	SSM	0.6 (4.9%)	4.0	<u>94.65 (+ 0.33)</u>	<u>93.14 (+ 0.54)</u>	<u>89.96 (+ 0.65)</u>	<u>93.5 (- 0.1)</u>
◦ Mamba3D[12]	ACM MM24	SSM	16.9 (100%)	3.9	93.12	92.08	<u>92.05</u>	<b>94.7</b>
+ PMA†[50]	CVPR25	SSM	1.3 (7.7%)	4.7	91.97 (- 1.15)	89.64 (- 2.44)	88.70 (- 3.35)	94.2 (- 0.5)
+ Mantis	<b>This Paper</b>	SSM	0.8 (4.7%)	4.0	93.29 (+ 0.17)	92.77 (+ 0.69)	<b>93.48 (+ 1.43)</b>	<b>94.7 (+ 0.0)</b>
◦ ZigzagPointMamba[7]	NeurIPS25	SSM	12.3 (100%)	3.1	94.15	92.10	88.65	93.2
+ PMA†[50]	CVPR25	SSM	1.1 (8.9%)	5.7	93.10 (- 1.05)	89.53 (- 2.57)	85.18 (- 3.47)	92.8 (- 0.4)
+ Mantis	<b>This Paper</b>	SSM	0.6 (4.9%)	4.5	94.02 (- 0.13)	<u>93.27 (+ 1.17)</u>	90.11 (+ 1.46)	93.7 (+ 0.5)

## 4.1 Object classification

**Real-World Object Classification.** The ScanObjectNN[36] dataset is a highly challenging 3D dataset covering  $\sim 15K$  real-world objects across 15 categories. As shown in Table 1, we conduct experiments on three variants of ScanObjectNN (*i.e.*, OBJ\_BG, OBJ\_ONLY, and PB\_T50\_RS), each with increasing complexity. Mantis surpasses the full fine-tuning in most cases with only about 5% of the parameters. Specifically, Mantis surpasses the full fine-tuning of PointMamba, Mamba3D, and ZigzagPointMamba by **0.65%**, **1.43%**, **1.46%** on PB\_T50\_RS split, respectively. Furthermore, the t-SNE feature visualization[37] of existing methods and Mantis are presented in Figure 4 (a). This suggests that Mantis is especially effective in improving robustness under noisy and order-sensitive real-world point cloud distributions. Notably, the more pronounced performance improvements on the most challenging PB\_T50\_RS split indicate that dynamic state-aware adaptation and cross-serialization consistency become increasingly beneficial when serialization-induced instability is amplified. A detailed analysis of this phenomenon is provided in Appendix C.2.

**Synthetic Object Classification.** The ModelNet40[45] dataset contains a total of 12,311 3D CAD models across 40 categories. Due to the computational cost of the voting strategy[26], we report overall accuracy without voting. As shown in Table 1, compared to full fine-tuning, Mantis substantially reduces resource requirements while achieving comparable performance.

**Few-shot Learning.** We further conduct few-shot experiments on ModelNet40[45] to assess our few-shot transfer learning ability. Following previous works[27], we employ the n-way, m-shot configuration with  $n \in \{5, 10\}$  and  $m \in \{10, 20\}$ . As shown in Table 2, our Mantis achieves the best or second-best accuracy in all configurations, indicating its effectiveness in few-shot learning.

Table 2: Few-shot learning on ModelNet40[45]. A Table 3: Part segmentation results on the dedicated dataset for few-shot learning constructed ShapeNetPart[46] dataset. The mIoU for all based on ModelNet40. We report the average accuracy (Cls.) and for all instances (Inst.) are racy (%)  $\pm$  the standard deviation (%) of 10 independent experiments without voting. \* denotes results reproduced from the public source code.

Methods	5-way		10-way		Methods	#TP (M)	Inst.mIoU	Cls.mIoU
	10-shot	20-shot	10-shot	20-shot				
<i>Self-Supervised Learning (Full Fine-tuning)</i>					<i>Self-Supervised Learning (Full Fine-tuning)</i>			
Point-BERT[47]	94.6 $\pm$ 3.1	96.3 $\pm$ 2.7	91.0 $\pm$ 5.4	92.7 $\pm$ 5.1	Point-BERT[47]	27.1	85.6	84.1
MaskPoint[25]	95.0 $\pm$ 3.7	97.2 $\pm$ 1.7	91.4 $\pm$ 4.0	93.4 $\pm$ 3.5	PointMAE[27]	27.1	86.1	84.1
Point-MAE[27]	96.3 $\pm$ 2.5	97.8 $\pm$ 1.8	92.6 $\pm$ 4.1	95.0 $\pm$ 3.0	ACT[8]	27.1	<u>86.1</u>	<b>84.7</b>
ReCon[30]	97.3 $\pm$ 1.9	98.9 $\pm$ 1.2	93.3 $\pm$ 3.9	93.3 $\pm$ 3.9	ReCon[30]	48.5	<b>86.4</b>	84.5
PointGPT-S[4]	<b>98.0<math>\pm</math>1.9</b>	<b>99.0<math>\pm</math>1.0</b>	<b>94.1<math>\pm</math>3.3</b>	<b>96.1<math>\pm</math>2.8</b>	<i>Self-Supervised Learning (Parameter-Efficient Fine-Tuning)</i>			
ACT[8]	96.8 $\pm$ 2.3	98.0 $\pm$ 1.4	93.3 $\pm$ 4.0	95.6 $\pm$ 2.8	PointMamba[23]	17.4	85.3	82.6
<i>Self-Supervised Learning (Parameter-Efficient Fine-Tuning)</i>					+ PMA*	8.3	84.2 (- 1.1)	82.3 (- 0.3)
PointMamba	96.9 $\pm$ 2.0	99.0 $\pm$ 1.1	93.0 $\pm$ 4.4	95.6 $\pm$ 3.2	+ <b>Mantis</b>	6.8	85.1 (- 0.2)	82.9 (+ 0.3)
+ <b>Mantis</b>	<u>97.2<math>\pm</math>1.9</u>	<b>99.0<math>\pm</math>1.0</b>	<u>93.4<math>\pm</math>4.0</u>	<b>96.4<math>\pm</math>3.1</b>	Mamba3D[12]	23.0	85.6	83.6
Mamba3D	96.4 $\pm$ 2.2	98.2 $\pm$ 1.2	92.4 $\pm$ 4.1	95.2 $\pm$ 2.9	+ PMA*	9.1	83.7 (- 1.9)	82.4 (- 1.2)
+ <b>Mantis</b>	95.3 $\pm$ 3.5	98.9 $\pm$ 2.4	91.7 $\pm$ 3.2	95.3 $\pm$ 3.2	+ <b>Mantis</b>	7.4	<u>86.1 (+ 0.5)</u>	<u>84.1 (+ 0.5)</u>
ZigzagPointMamba	96.0 $\pm$ 2.1	99.0 $\pm$ 1.2	90.0 $\pm$ 2.2	94.2 $\pm$ 1.0	ZigzagPointMamba[7]	17.4	85.8	84.2
+ <b>Mantis</b>	96.2 $\pm$ 1.6	<u>99.0<math>\pm</math>1.1</u>	92.8 $\pm$ 2.1	95.5 $\pm$ 4.6	+ PMA*	8.3	84.1 (- 1.7)	82.0 (- 2.2)
					+ <b>Mantis</b>	6.8	85.9 (+ 0.1)	<u>84.5 (+ 0.3)</u>

Table 4: Ablation study on the setting of Mantis, including different components, inserted layers and PEFT methods. The details of the table are described in Sec. 4.3.

(a) The effect of each component. (b) The effect of inserted layers. (c) The effect of different PEFT methods.

SAA	DSCD		#TP (M)	PB_T50_RS	Layers	#TP (M)	PB_T50_RS	Methods	#TP (M)	PB_T50_RS
	$\mathcal{L}_{feat}$	$\mathcal{L}_{pred}$								
<i>Vanilla Protocol</i>					<i>Vanilla Protocol</i>					
			16.9	92.05	1 $\rightarrow$ 3	0.50	88.74	+ Adapter[15]	0.87	84.45 (- 7.60)
			0.27	80.84	1 $\rightarrow$ 6	0.61	90.12	+ Prefix tuning[21]	0.71	83.26 (- 8.79)
					1 $\rightarrow$ 9	0.72	91.56	+ LoRA[16]	0.91	83.19 (- 8.86)
<i>Mantis Protocol</i>					<i>Mantis Protocol</i>					
	✓		0.38	84.12	1 $\rightarrow$ 12	0.84	<b>93.48</b>	+ VPT-Deep[17]	0.41	83.37 (- 8.68)
		✓	0.38	83.95	4 $\rightarrow$ 6	0.50	89.21	+ AdaptFormer[5]	0.87	84.13 (- 7.92)
	✓	✓	0.38	84.53	4 $\rightarrow$ 9	0.61	90.37	+ BI-AdaptFormer[19]	0.87	82.88 (- 9.17)
			0.72	91.86	4 $\rightarrow$ 12	0.72	92.04			
✓			0.84	92.61	7 $\rightarrow$ 9	0.50	88.63	+ PointLoRA[16]	0.77	85.36 (- 6.69)
✓	✓		0.84	92.38	7 $\rightarrow$ 12	0.61	89.72	+ PointGST[24]	0.62	87.38 (- 4.67)
✓		✓	0.84	92.38	10 $\rightarrow$ 12	0.50	88.11	+ <b>Mantis</b>	0.84	<b>93.48 (+ 1.43)</b>
✓	✓	✓	0.84	<b>93.48</b>						

## 4.2 Part segmentation

We conduct part segmentation experiments on the challenging ShapeNetPart[46] dataset, which includes 16,881 samples from 16 categories and 50 part labels. As shown in Table 3, in this fine-grained scene understanding task, our approach still achieves competitive results on Inst. mIoU and notable improvements on Cls. mIoU compared with full fine-tuning. Qualitatively, as shown in Figure 4 (b), Mantis produces more accurate and coherent part boundaries than baselines, especially for small or structurally complex parts. Similar to the observations on the most challenging ScanObjectNN split, the advantage of Mantis is more pronounced in this fine-grained setting, indicating its effectiveness in robustly modeling subtle part-level geometric structures. Distinct from prior classification models, the increase in the parameter count is primarily attributed to the segmentation head.

## 4.3 Ablation study

We conduct ablation studies on the most challenging PB\_T50\_RS variant based on Mamba3D[12] to investigate the rationale and effectiveness of Mantis. More results are provided in Appendix B.2.

**Ablation on different components.** We first study the contribution of each component in Mantis. As illustrated in Table 4 (a), SAA constitutes the primary source of performance improvement. DSCD alone provides modest improvement, whereas the introduction of SAA leads to substantial gain. Building on SAA, both feature consistency and prediction consistency bring further gains, and their combination achieves the best result. Overall, DSCD functions as a regularizer that complements SAA, while feature-level and prediction-level consistency provide complementary benefits.

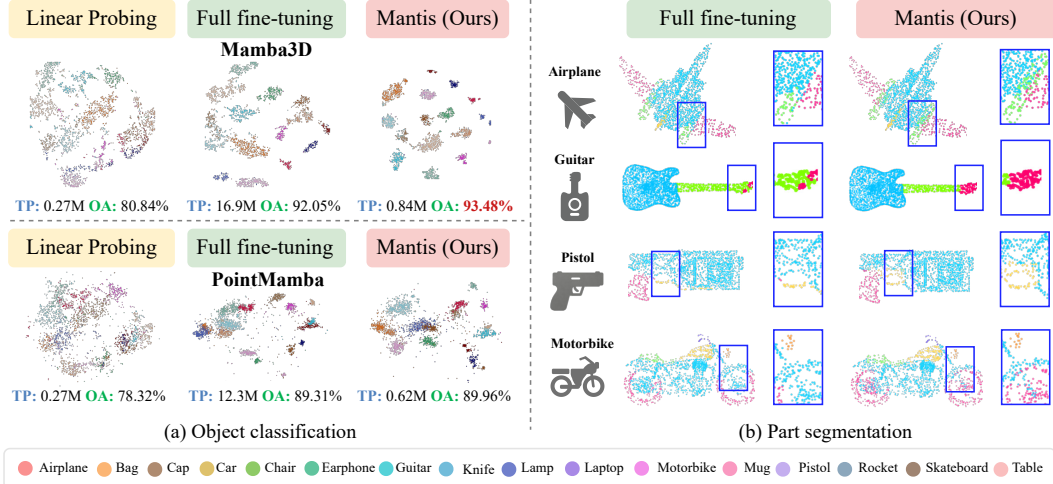


Figure 4: **Qualitative analysis results for object classification and part segmentation.** (a) The t-SNE visualization results on the PB\_T50\_RS variant with different fine-tuning schemes. (b) Comparison of full fine-tuning and Mantis on part segmentation with Mamba3D[12].

**Ablation on different inserted layers.** One straightforward way to further reduce the number of tunable parameters is to insert SAA into only a subset of encoder layers rather than the full network. However, as illustrated in Table 4 (b), restricting SAA to partial layers consistently degrades performance, regardless of whether the selected layers are shallow, intermediate, or deep. This observation suggests that effective adaptation of a frozen Mamba backbone requires state modulation across all encoder layers, rather than within a few isolated layers. When SAA is limited to middle or late layers, the performance drops noticeably, indicating that suboptimal state evolution formed in earlier stages cannot be adequately compensated by later-layer correction.

**Ablation on different PEFT methods.** To further validate the effectiveness of our proposed method, we compare Mantis with several representative PEFT approaches originally developed for NLP[15, 21, 16], 2D vision[17, 5, 19], and 3D point clouds[24, 40]. As illustrated in Table 4 (c), although these methods introduce different forms of parameter-efficient adaptation, they all suffer from substantial performance degradation compared with full fine-tuning. This suggests that existing PEFT strategies, even those tailored for point clouds, remain insufficient to effectively adapt frozen Mamba backbones. A possible reason is that most of them are designed for token-wise interactions or feature transformation, and therefore cannot properly align with the state-space dynamics and serialization-sensitive modeling mechanism of Mamba. In contrast, the strength of Mantis lies not merely in parameter efficiency, but in its Mamba-native design that better matches the intrinsic adaptation demands of selective SSMs.

## 5 Limitations

While Mantis achieves promising results across various benchmarks, several limitations warrant acknowledgment. First, Mantis depends on manually designed configurations, which may limit its performance across different downstream tasks. Second, Mantis focuses on single-modal point cloud inputs. Incorporating complementary modalities, such as images or language, into a Mamba-native PEFT framework remains a promising but underexplored direction. We leave these for future research.

## 6 Conclusion

In this paper, we propose Mantis, the first Mamba-native PEFT framework for 3D PFMs. We identify the mismatch between existing Transformer-native PEFT methods and Mamba-based backbones, and address it through state-level adaptation and cross-serialization regularization. Extensive experiments demonstrate that our Mantis achieves strong downstream performance with only about 5% of trainable parameters. As an early exploration of Mamba-native PEFT, we expect Mantis can serve as a baseline and provide insights for future 3D PEFT research.

## References

- [1] Zixiang Ai, Zichen Liu, Yuanhang Lei, Zhenyu Cui, Xu Zou, and Jiahuan Zhou. GAPrompt: Geometry-aware point cloud prompt for 3D vision model. In *Proceedings of the 42nd International Conference on Machine Learning (ICML)*, 2025.
- [2] Iro Armeni, Ozan Sener, Amir R. Zamir, Helen Jiang, Ioannis Brilakis, Martin Fischer, and Silvio Savarese. 3d semantic parsing of large-scale indoor spaces. In *Proceedings of the IEEE Conference on Computer Vision and Pattern Recognition (CVPR)*, 2016.
- [3] Ali Bahri, Moslem Yazdanpanah, Mehrdad Noori, Sahar Dastani, Milad Cheraghali, Gustavo Adolfo Vargas Hakim, David Osowiechi, Farzad Beizae, Ismail Ben Ayed, and Christian Desrosiers. Spectral informed mamba for robust point cloud processing. In *Proceedings of the Computer Vision and Pattern Recognition Conference (CVPR)*, 2025.
- [4] Guangyan Chen, Meiling Wang, Yi Yang, Kai Yu, Li Yuan, and Yufeng Yue. Pointgpt: Auto-regressively generative pre-training from point clouds. *Advances in Neural Information Processing Systems (NeurIPS)*, 2023.
- [5] Shoufa Chen, Chongjian Ge, Zhan Tong, Jiangliu Wang, Yibing Song, Jue Wang, and Ping Luo. Adaptformer: Adapting vision transformers for scalable visual recognition. *Advances in Neural Information Processing Systems (NeurIPS)*, 2022.
- [6] Jacob Devlin, Ming-Wei Chang, Kenton Lee, and Kristina Toutanova. Bert: Pre-training of deep bidirectional transformers for language understanding. In *Proceedings of the 2019 conference of the North American chapter of the association for computational linguistics: human language technologies, volume 1 (NAACL)*, 2019.
- [7] Linshuang Diao, Sensen Song, Yurong Qian, and Dayong Ren. Zigzagpointmamba: Spatial-semantic mamba for point cloud understanding. In *Advances in Neural Information Processing Systems (NeurIPS)*, 2025.
- [8] Runpei Dong, Zekun Qi, Linfeng Zhang, Junbo Zhang, Jianjian Sun, Zheng Ge, Li Yi, and Kaisheng Ma. Autoencoders as cross-modal teachers: Can pretrained 2d image transformers help 3d representation learning? In *The Eleventh International Conference on Learning Representations (ICLR)*, 2023.
- [9] Albert Gu and Tri Dao. Mamba: Linear-time sequence modeling with selective state spaces. In *First conference on language modeling (COLM)*, 2024.
- [10] Albert Gu, Karan Goel, and Christopher Re. Efficiently modeling long sequences with structured state spaces. In *International Conference on Learning Representations (ICLR)*, 2022.
- [11] Ziyu Guo, Renrui Zhang, Longtian Qiu, Xianzhi Li, and Pheng-Ann Heng. Joint-mae: 2d-3d joint masked autoencoders for 3d point cloud pre-training. In *Proceedings of the Thirty-Second International Joint Conference on Artificial Intelligence (IJCAI)*, 2023.
- [12] Xu Han, Yuan Tang, Zhaoxuan Wang, and Xianzhi Li. Mamba3d: Enhancing local features for 3d point cloud analysis via state space model. In *Proceedings of the 32nd ACM International Conference on Multimedia (ACM MM)*, 2024.
- [13] Xu Han, Yuan Tang, Jinfeng Xu, and Xianzhi Li. Most: Efficient monarch sparse tuning for 3d representation learning. In *Proceedings of the Computer Vision and Pattern Recognition Conference (CVPR)*, 2025.
- [14] David Hilbert. Über die stetige abbildung einer linie auf ein flächenstück. In *Dritter Band: Analysis· Grundlagen der Mathematik· Physik Verschiedenes: Nebst Einer Lebensgeschichte*. Springer, 1935.
- [15] Neil Houlsby, Andrei Giurgiu, Stanislaw Jastrzebski, Bruna Morrone, Quentin De Laroussilhe, Andrea Gesmundo, Mona Attariyan, and Sylvain Gelly. Parameter-efficient transfer learning for nlp. In *International conference on machine learning (ICML)*, 2019.

- [16] Edward J Hu, Yelong Shen, Phillip Wallis, Zeyuan Allen-Zhu, Yuanzhi Li, Shean Wang, Lu Wang, and Weizhu Chen. LoRA: Low-rank adaptation of large language models. In *International Conference on Learning Representations (ICLR)*, 2022.
- [17] Menglin Jia, Luming Tang, Bor-Chun Chen, Claire Cardie, Serge Belongie, Bharath Hariharan, and Ser-Nam Lim. Visual prompt tuning. In *European conference on computer vision (ECCV)*. Springer, 2022.
- [18] Zhaoyi Jiang, Yi Xu, Frederick W.B. Li, Gary K.L. Tam, Chao Song, and Bailin Yang. Octmamba: Mamba-based octree context entropy model for point cloud geometry compression. *Pattern Recognition (PR)*, 2026.
- [19] Shibo Jie, Haoqing Wang, and Zhi-Hong Deng. Revisiting the parameter efficiency of adapters from the perspective of precision redundancy. In *Proceedings of the IEEE/CVF international conference on computer vision (ICCV)*, 2023.
- [20] Pengbo Li, Yiding Sun, and Haozhe Cheng. Pointdico: Contrastive 3d representation learning guided by diffusion models. In *2025 International Joint Conference on Neural Networks (IJCNN)*, 2025.
- [21] Xiang Lisa Li and Percy Liang. Prefix-tuning: Optimizing continuous prompts for generation. In *Proceedings of the 59th Annual Meeting of the Association for Computational Linguistics and the 11th International Joint Conference on Natural Language Processing (Volume 1: Long Papers) (ACL)*, 2021.
- [22] Yangyan Li, Rui Bu, Mingchao Sun, Wei Wu, Xinhan Di, and Baoquan Chen. Pointcnn: Convolution on x-transformed points. *Advances in neural information processing systems (NeurIPS)*, 2018.
- [23] Dingkan Liang, Xin Zhou, Wei Xu, Xingkui Zhu, Zhikang Zou, Xiaoqing Ye, Xiao Tan, and Xiang Bai. Pointmamba: A simple state space model for point cloud analysis. In *Advances in Neural Information Processing Systems (NeurIPS)*, 2024.
- [24] Dingkan Liang, Tianrui Feng, Xin Zhou, Yumeng Zhang, Zhikang Zou, and Xiang Bai. Parameter-efficient fine-tuning in spectral domain for point cloud learning. *IEEE transactions on pattern analysis and machine intelligence (TPAMI)*, 2025.
- [25] Haotian Liu, Mu Cai, and Yong Jae Lee. Masked discrimination for self-supervised learning on point clouds. In *European Conference on Computer Vision (ECCV)*. Springer, 2022.
- [26] Yongcheng Liu, Bin Fan, Shiming Xiang, and Chunhong Pan. Relation-shape convolutional neural network for point cloud analysis. In *Proceedings of the IEEE/CVF conference on computer vision and pattern recognition (CVPR)*, 2019.
- [27] Yatian Pang, Wenxiao Wang, Francis E. H. Tay, Wei Liu, Yijun Tian, and Li Yuan. Masked autoencoders for point cloud self-supervised learning. In *European Conference on Computer Vision (ECCV)*, 2022.
- [28] Charles R. Qi, Hao Su, Kaichun Mo, and Leonidas J. Guibas. Pointnet: Deep learning on point sets for 3d classification and segmentation. In *Proceedings of the IEEE Conference on Computer Vision and Pattern Recognition (CVPR)*, 2017.
- [29] Charles R. Qi, Li Yi, Hao Su, and Leonidas J. Guibas. Pointnet++: Deep hierarchical feature learning on point sets in a metric space. In *Advances in Neural Information Processing Systems (NeurIPS)*, 2017.
- [30] Zekun Qi, Runpei Dong, Guofan Fan, Zheng Ge, Xiangyu Zhang, Kaisheng Ma, and Li Yi. Contrast with reconstruct: Contrastive 3d representation learning guided by generative pretraining. In *Proceedings of the 40th International Conference on Machine Learning (ICML)*, 2023.
- [31] Kanglin Qu, Pan Gao, Qun Dai, and Yuanhao Sun. Hydramamba: Multi-head state space model for global point cloud learning. In *Proceedings of the 33rd ACM International Conference on Multimedia (ACM MM)*, 2025.

- [32] Kanglin Qu, Pan Gao, Qun Dai, Zhanzhi Ye, Rui Ye, and Yuanhao Sun. Cloudmamba: Grouped selective state spaces for point cloud analysis. In *Proceedings of the AAAI Conference on Artificial Intelligence (AAAI)*, 2026.
- [33] Yiding Sun, Haozhe Cheng, Chaoyi Lu, Zhengqiao Li, Minghong Wu, Huimin Lu, and Jihua Zhu. Hyperpoint: Multimodal 3d foundation model in hyperbolic space. *Pattern Recognition (PR)*, 2026.
- [34] Yiding Sun, Jihua Zhu, Haozhe Cheng, Chaoyi Lu, Zhichuan Yang, Lin Chen, and Yaonan Wang. Align then adapt: Rethinking parameter-efficient transfer learning in 4d perception. *arXiv preprint arXiv:2602.23069*, 2026.
- [35] Yiwen Tang, Ray Zhang, Zoey Guo, Xianzheng Ma, Bin Zhao, Zhigang Wang, Dong Wang, and Xuelong Li. Point-peft: Parameter-efficient fine-tuning for 3d pre-trained models. In *Proceedings of the AAAI Conference on Artificial Intelligence (AAAI)*, 2024.
- [36] Mikaela Angelina Uy, Quang-Hieu Pham, Binh-Son Hua, Duc Thanh Nguyen, and Sai-Kit Yeung. Revisiting point cloud classification: A new benchmark dataset and classification model on real-world data. In *International Conference on Computer Vision (ICCV)*, 2019.
- [37] Laurens van der Maaten and Geoffrey Hinton. Visualizing data using t-sne. *Journal of Machine Learning Research (JMLR)*, 2008.
- [38] Ashish Vaswani, Noam Shazeer, Niki Parmar, Jakob Uszkoreit, Llion Jones, Aidan N Gomez, Łukasz Kaiser, and Illia Polosukhin. Attention is all you need. In *Advances in neural information processing systems (NeurIPS)*, 2017.
- [39] Chuxin Wang, Yixin Zha, Wenfei Yang, and Tianzhu Zhang. Strumamba3d: Exploring structural mamba for self-supervised point cloud representation learning. In *Proceedings of the IEEE/CVF International Conference on Computer Vision (ICCV)*, 2025.
- [40] Song Wang, Xiaolu Liu, Lingdong Kong, Jianyun Xu, Chunyong Hu, Gongfan Fang, Wentong Li, Jianke Zhu, and Xinchao Wang. Pointlora: Low-rank adaptation with token selection for point cloud learning. In *Proceedings of the IEEE/CVF Conference on Computer Vision and Pattern Recognition (CVPR)*, 2025.
- [41] Yankai Wang, Yiding Sun, Qirui Wang, Pengbo Li, Chaoyi Lu, and Dongxu Zhang. Pointrft: Explicit reinforcement fine-tuning for point cloud few-shot learning. *arXiv preprint arXiv:2603.23957*, 2026.
- [42] Yue Wang, Yongbin Sun, Ziwei Liu, Sanjay E. Sarma, Michael M. Bronstein, and Justin M. Solomon. Dynamic graph cnn for learning on point clouds. *ACM Transactions on Graphics (TOG)*, 2019.
- [43] Xiaoyang Wu, Yixing Lao, Li Jiang, Xihui Liu, and Hengshuang Zhao. Point transformer v2: Grouped vector attention and partition-based pooling. In *Advances in Neural Information Processing Systems (NeurIPS)*, 2022.
- [44] Xiaoyang Wu, Yuxin Lao, Li Jiang, Xiangyu Liu, and Hengshuang Zhao. Point transformer v3: Simpler, faster, stronger. In *Proceedings of the IEEE/CVF conference on Computer Vision and Pattern Recognition (CVPR)*, 2024.
- [45] Zhirong Wu, Shuran Song, Aditya Khosla, Fisher Yu, Linguang Zhang, Xiaoou Tang, and Jianxiong Xiao. 3d shapenets: A deep representation for volumetric shapes. In *Proceedings of the IEEE Conference on Computer Vision and Pattern Recognition (CVPR)*, 2015.
- [46] Li Yi, Vladimir G. Kim, Duygu Ceylan, I Chao Shen, Mengyan Yan, Hao Su, Cewu Lu, Qixing Huang, Alla Sheffer, and Leonidas Guibas. A scalable active framework for region annotation in 3d shape collections. *ACM Transactions on Graphics (TOG)*, 2016.
- [47] Xiaoyang Yu, Yilun Tang, Yue Rao, Tiejun Huang, Jie Zhou, and Jiwen Lu. Point-bert: Pre-training 3d point cloud transformers with masked point modeling. In *Proceedings of the IEEE/CVF Conference on Computer Vision and Pattern Recognition (CVPR)*, 2022.

- [48] Yaohua Zha, Jinpeng Wang, Tao Dai, Bin Chen, Zhi Wang, and Shu-Tao Xia. Instance-aware dynamic prompt tuning for pre-trained point cloud models. In *Proceedings of the IEEE/CVF International Conference on Computer Vision (ICCV)*, 2023.
- [49] Yaohua Zha, Huizhen Ji, Jinmin Li, Rongsheng Li, Tao Dai, Bin Chen, Zhi Wang, and Shu-Tao Xia. Towards compact 3d representations via point feature enhancement masked autoencoders. In *Proceedings of the AAAI Conference on Artificial Intelligence (AAAI)*, 2024.
- [50] Yaohua Zha, Yanzi Wang, Hang Guo, Jinpeng Wang, Tao Dai, Bin Chen, Zhihao Ouyang, Xue Yuerong, Ke Chen, and Shu-Tao Xia. Pma: Towards parameter-efficient point cloud understanding via point mamba adapter. In *Proceedings of the Computer Vision and Pattern Recognition Conference (CVPR)*, 2025.
- [51] Yixin Zha, Chuxin Wang, Wenfei Yang, Tianzhu Zhang, and Feng Wu. Exploring vision semantic prompt for efficient point cloud understanding. In *Proceedings of the 42nd International Conference on Machine Learning (ICML)*, 2025.
- [52] Dongxu Zhang, Yiding Sun, Pengcheng Li, Yumou Liu, Hongqiang Lin, Haoran Xu, Xiaoxuan Mu, Liang Lin, Wenbiao Yan, Ning Yang, et al. Pointcot: A multi-modal benchmark for explicit 3d geometric reasoning. *arXiv preprint arXiv:2602.23945*, 2026.
- [53] Renrui Zhang, Ziyu Guo, Peng Gao, Rongyao Fang, Bin Zhao, Dong Wang, Yu Qiao, and Hongsheng Li. Point-m2ae: Multi-scale masked autoencoders for hierarchical point cloud pre-training. In *Advances in Neural Information Processing Systems (NeurIPS)*, 2022.
- [54] Renrui Zhang, Liuhui Wang, Yu Qiao, Peng Gao, and Hongsheng Li. Learning 3d representations from 2d pre-trained models via image-to-point masked autoencoders. In *Proceedings of the IEEE/CVF conference on computer vision and pattern recognition (CVPR)*, 2023.
- [55] Tao Zhang, Haobo Yuan, Lu Qi, Jiangning Zhang, Qianyu Zhou, Shunping Ji, Shuicheng Yan, and Xiangtai Li. Point cloud mamba: Point cloud learning via state space model. In *Proceedings of the AAAI Conference on Artificial Intelligence (AAAI)*, 2025.
- [56] Hengshuang Zhao, Li Jiang, Jiaya Jia, Philip H. S. Torr, and Vladlen Koltun. Point transformer. In *Proceedings of the IEEE/CVF International Conference on Computer Vision (ICCV)*, 2021.
- [57] Xin Zhou, Ding kang Liang, Wei Xu, Xingkui Zhu, Yihan Xu, Zhikang Zou, and Xiang Bai. Dynamic adapter meets prompt tuning: Parameter-efficient transfer learning for point cloud analysis. In *Proceedings of the IEEE/CVF Conference on Computer Vision and Pattern Recognition (CVPR)*, 2024.

## Appendix Table of Contents

<b>A</b>	<b>Additional theoretical analysis</b> . . . . .	<b>15</b>
A.1	A closer look at selective SSM under serialization . . . . .	15
A.2	Effect of State-Aware Adapter on selective state-space dynamics. . . . .	16
A.3	Parameter and complexity analysis . . . . .	17
<b>B</b>	<b>More experimental results</b> . . . . .	<b>17</b>
B.1	Training detail . . . . .	17
B.2	Additional ablation study. . . . .	18
B.3	Large-scale indoor scene semantic segmentation . . . . .	20
B.4	Detailed results for classification and segmentation. . . . .	20
B.5	Part segmentation visualization . . . . .	20
<b>C</b>	<b>Explanatory experiments and discussions</b> . . . . .	<b>21</b>
C.1	Training dynamics and optimization stability. . . . .	21
C.2	Further analysis on PB_T50_RS . . . . .	22
C.3	Discussion on the scope of Mamba-native adaptation . . . . .	23
<b>D</b>	<b>Symbol table</b> . . . . .	<b>24</b>

## A Additional theoretical analysis

### A.1 A closer look at selective SSM under serialization

Different from LTI SSMs with fixed transition kernels, Mamba uses input-dependent operators. For point cloud modeling, when the same point cloud is serialized into different valid orders, both the input sequence and the induced operator chains change. Consequently, the effective transfer kernel becomes inherently dependent on the chosen serialization.

As described in Sec. 3.1, for branch  $k \in \{1, 2\}$ , the selective state-space model updates the hidden state according to

$$h_t^{(k)} = \widehat{\mathbf{A}}_t^{(k)} h_{t-1}^{(k)} + \widehat{\mathbf{B}}_t^{(k)} x_t^{(k)}, \quad y_t^{(k)} = \widetilde{\mathbf{C}}_t^{(k)} h_t^{(k)}, \quad (15)$$

where  $x_t^{(k)} \in \mathbb{R}^d$  is the input token at step  $t$ ,  $h_t^{(k)} \in \mathbb{R}^{d_h}$  is the hidden state,  $\widehat{\mathbf{A}}_t^{(k)}$  and  $\widehat{\mathbf{B}}_t^{(k)}$  denote the discretized input-dependent transition and input operators, respectively, and  $\widetilde{\mathbf{C}}_t^{(k)}$  denotes the corresponding controlled readout operator.

Ignoring the initial state for simplicity, the recurrent form in Eq. (15) can be expanded as:

$$h_t^{(k)} = \sum_{i=1}^t \left( \prod_{j=i+1}^t \widehat{\mathbf{A}}_j^{(k)} \right) \widehat{\mathbf{B}}_i^{(k)} x_i^{(k)}, \quad (16)$$

where the product is defined in temporal order, *i.e.*,  $\prod_{j=i+1}^t \widehat{\mathbf{A}}_j^{(k)} = \widehat{\mathbf{A}}_t^{(k)} \widehat{\mathbf{A}}_{t-1}^{(k)} \cdots \widehat{\mathbf{A}}_{i+1}^{(k)}$ , and equals the identity matrix when  $i = t$ .

Substituting Eq. (16) into the readout equation yields:

$$y_t^{(k)} = \sum_{i=1}^t \widetilde{\mathbf{C}}_t^{(k)} \left( \prod_{j=i+1}^t \widehat{\mathbf{A}}_j^{(k)} \right) \widehat{\mathbf{B}}_i^{(k)} x_i^{(k)}. \quad (17)$$

Thus, the selective transfer kernel from step  $i$  to step  $t$  is defined as:

$$\mathbf{W}_{t,i}^{(k)} = \widetilde{\mathbf{C}}_t^{(k)} \left( \prod_{j=i+1}^t \widehat{\mathbf{A}}_j^{(k)} \right) \widehat{\mathbf{B}}_i^{(k)}, \quad 1 \leq i \leq t \leq n, \quad (18)$$

where  $n$  is the serialized sequence length. Then Eq. (17) can be rewritten as:

$$y_t^{(k)} = \sum_{i=1}^t \mathbf{W}_{t,i}^{(k)} x_i^{(k)}. \quad (19)$$

Stacking all outputs  $\hat{\mathbf{y}}^{(k)} = [y_1^{(k)}, \dots, y_n^{(k)}]^\top$  and inputs  $\hat{\mathbf{x}}^{(k)} = [x_1^{(k)}, \dots, x_n^{(k)}]^\top$ , Eq. (19) can be expressed in matrix form:

$$\hat{\mathbf{y}}^{(k)} = \mathbf{W}^{(k)} \hat{\mathbf{x}}^{(k)}, \quad \mathbf{W}^{(k)} = \begin{bmatrix} \mathbf{W}_{1,1}^{(k)} & 0 & \cdots & 0 \\ \mathbf{W}_{2,1}^{(k)} & \mathbf{W}_{2,2}^{(k)} & \cdots & 0 \\ \vdots & \vdots & \ddots & \vdots \\ \mathbf{W}_{n,1}^{(k)} & \mathbf{W}_{n,2}^{(k)} & \cdots & \mathbf{W}_{n,n}^{(k)} \end{bmatrix}. \quad (20)$$

Since  $\mathbf{W}^{(k)}$  is lower triangular, the selective SSM defines a causal, input-dependent transfer matrix over the serialized point sequence.

Eq. (20) also reveals the source of serialization sensitivity. For two valid serializations of the same point cloud, not only the input order  $\hat{\mathbf{x}}^{(1)}$  and  $\hat{\mathbf{x}}^{(2)}$  differ, but the induced operator chains  $\prod_{j=i+1}^t \widehat{\mathbf{A}}_j^{(1)}$  and  $\prod_{j=i+1}^t \widehat{\mathbf{A}}_j^{(2)}$  also differ. Consequently, the same underlying geometry may lead to different transfer matrices and hence different representations under distinct valid serializations.

## A.2 Effect of State-Aware Adapter on selective state-space dynamics

To characterize the state-level adaptation mechanism of SAA, we analyze its effect on the selective transfer kernel of the frozen Mamba backbone. Building on the selective transfer kernel derived in Appendix A.1,  $\mathbf{W}_{t,i}^{(k)}$  denotes the selective transfer kernel after SAA modulation, while  $\mathbf{W}_{t,i}^{(k,0)}$  denotes its frozen counterpart without SAA:

$$\mathbf{W}_{t,i}^{(k,0)} = \mathbf{C}_t^{(k)} \left( \prod_{j=i+1}^t \overline{\mathbf{A}}_j^{(k)} \right) \overline{\mathbf{B}}_i^{(k)}, \quad (21)$$

where  $\overline{\mathbf{A}}_t^{(k)}$  and  $\overline{\mathbf{B}}_t^{(k)}$  are the discretized operators of the original frozen selective SSM, and  $\mathbf{C}_t^{(k)}$  is the corresponding readout matrix. Under SAA, the operator modulation takes the form:

$$\delta_t^{(k)} = \mathbf{U} \operatorname{diag}(\mathbf{u}_t^{(k)}) \mathbf{V}, \quad (22)$$

where  $\mathbf{u}_t^{(k)} \in \mathbb{R}^r$  is the sparse control signal, and  $\mathbf{U}$  and  $\mathbf{V}$  are learnable low-rank matrices. This perturbation is partitioned and added to  $\mathbf{A}_t^{(k)}$ ,  $\mathbf{B}_t^{(k)}$ ,  $\mathbf{C}_t^{(k)}$ , and  $\mathbf{\Delta}_t^{(k)}$ , which yields the controlled kernel

$$\mathbf{W}_{t,i}^{(k)} = \tilde{\mathbf{C}}_t^{(k)} \left( \prod_{j=i+1}^t \widehat{\mathbf{A}}_j^{(k)} \right) \widehat{\mathbf{B}}_i^{(k)}. \quad (23)$$

The corresponding kernel perturbation is

$$\Delta \mathbf{W}_{t,i}^{(k)} = \mathbf{W}_{t,i}^{(k)} - \mathbf{W}_{t,i}^{(k,0)}. \quad (24)$$

For each branch  $k$  and sequence step  $t$ , the perturbation  $\delta_t^{(k)} = \mathbf{U} \operatorname{diag}(\mathbf{u}_t^{(k)}) \mathbf{V}$  has rank at most  $|\mathbf{u}_t^{(k)}|_0$ . The key point is that  $\operatorname{diag}(\mathbf{u}_t^{(k)})$  contains exactly  $|\mathbf{u}_t^{(k)}|_0$  non-zero diagonal entries, while multiplication by  $\mathbf{U}$  and  $\mathbf{V}$  preserves the rank upper bound. Since  $|\mathbf{u}_t^{(k)}|_0 \leq r$ , it follows that:

$$\operatorname{rank}(\delta_t^{(k)}) \leq r. \quad (25)$$

Therefore, SAA changes the selective transfer kernel through a sparse low-rank perturbation. The resulting adaptation is restricted to a limited subspace. This helps explain both the parameter efficiency and the stability of SAA on top of a frozen Mamba backbone: the pretrained state dynamics are not freely altered, but only adjusted through a controlled low-rank correction.

We further examine how the sparse low-rank perturbation affects the hidden-state trajectory. The hidden states produced by the frozen backbone and the SAA-modulated backbone are denoted as  $h_t^{(k,0)}$  and  $h_t^{(k)}$ , respectively:

$$h_t^{(k,0)} = \overline{\mathbf{A}}_t^{(k)} h_{t-1}^{(k,0)} + \overline{\mathbf{B}}_t^{(k)} x_t^{(k)}, \quad h_t^{(k)} = \widehat{\mathbf{A}}_t^{(k)} h_{t-1}^{(k)} + \widehat{\mathbf{B}}_t^{(k)} x_t^{(k)}. \quad (26)$$

The hidden-state deviation is defined as

$$\delta h_t^{(k)} = h_t^{(k)} - h_t^{(k,0)}. \quad (27)$$

Subtracting the frozen recurrence from the SAA-modulated recurrence gives

$$\delta h_t^{(k)} = \overline{\mathbf{A}}_t^{(k)} \delta h_{t-1}^{(k)} + \left( \widehat{\mathbf{A}}_t^{(k)} - \overline{\mathbf{A}}_t^{(k)} \right) h_{t-1}^{(k)} + \left( \widehat{\mathbf{B}}_t^{(k)} - \overline{\mathbf{B}}_t^{(k)} \right) x_t^{(k)}. \quad (28)$$

Assume that the frozen transition is contractive, *i.e.*,  $\|\overline{\mathbf{A}}_t^{(k)}\|_2 \leq \rho < 1$ , and the SAA-induced perturbations are bounded by  $\|\widehat{\mathbf{A}}_t^{(k)} - \overline{\mathbf{A}}_t^{(k)}\|_2 \leq \varepsilon_A$  and  $\|\widehat{\mathbf{B}}_t^{(k)} - \overline{\mathbf{B}}_t^{(k)}\|_2 \leq \varepsilon_B$ . Under the additional boundedness conditions  $\|h_t^{(k)}\|_2 \leq H$  and  $\|x_t^{(k)}\|_2 \leq X$  for all  $t$ , the deviation is bounded by

$$\|\delta h_t^{(k)}\|_2 \leq \rho \|\delta h_{t-1}^{(k)}\|_2 + \varepsilon_A H + \varepsilon_B X. \quad (29)$$

Unrolling the recursion yields

$$\left\| \delta h_t^{(k)} \right\|_2 \leq \rho^t \left\| \delta h_0^{(k)} \right\|_2 + \frac{1 - \rho^t}{1 - \rho} (\varepsilon_A H + \varepsilon_B X). \quad (30)$$

Eq. (30) shows that the hidden-state deviation is governed by the perturbation magnitudes  $\varepsilon_A$  and  $\varepsilon_B$ , and remains controlled when the SAA-induced operator perturbations are small. This suggests that SAA adapts the pretrained state dynamics in a controlled manner. Specifically, the selective transfer kernel is adjusted through sparse low-rank perturbations, while the induced hidden-state deviation remains bounded when the operator perturbations are small.

### A.3 Parameter and complexity analysis

We finally analyze the additional parameter and computational overhead introduced by the proposed State-Aware Adapter (SAA). Recall that SAA consists of the control projections  $W_x^\phi$ ,  $W_h^\phi$ , and  $W_e^\phi$ , the state fusion process  $\Phi(\cdot)$ , the driving and gating projections  $W_{\text{drv}}^\psi$  and  $W_{\text{gt}}^\psi$ , and the low-rank modulation matrices  $\mathbf{U}$  and  $\mathbf{V}$ . Accordingly, the total number of trainable parameters in one SAA module is

$$|\Theta_{\text{SAA}}| = |W_x^\phi| + |W_h^\phi| + |W_e^\phi| + |\Theta_\Phi| + |W_{\text{drv}}^\psi| + |W_{\text{gt}}^\psi| + |\mathbf{U}| + |\mathbf{V}|. \quad (31)$$

Specifically,  $W_x^\phi, W_e^\phi \in \mathbb{R}^{d_\phi \times d}$ ,  $W_h^\phi \in \mathbb{R}^{d_\phi \times d_h}$ , and  $W_{\text{drv}}^\psi, W_{\text{gt}}^\psi \in \mathbb{R}^{r \times d_\phi}$ . In our implementation, the state fusion process  $\Phi(\cdot)$  is instantiated as a lightweight MLP that projects the concatenated  $3d_\phi$ -dimensional control feature into the shared  $d_\phi$ -dimensional control space. For the low-rank modulation, we denote  $\mathbf{U} \in \mathbb{R}^{m \times r}$  and  $\mathbf{V} \in \mathbb{R}^{r \times m}$ , where  $m$  is the dimensionality of the operator space being modulated and  $r$  is the bottleneck dimension. The total number of trainable parameters in one SAA module therefore becomes

$$|\Theta_{\text{SAA}}| = 2d_\phi d + d_\phi d_h + 3d_\phi^2 + d_\phi + 2rd_\phi + 2mr. \quad (32)$$

Eq. (32) shows that the adaptation overhead is dominated by low-dimensional control projections and low-rank modulation. Since  $r \ll d$  and  $d_\phi$  is small, the number of trainable parameters introduced by SAA remains much smaller than that of full fine-tuning.

We next analyze the computational complexity. The additional overhead of SAA mainly comes from four parts: control-feature projection, state fusion, sparse control generation, and low-rank operator modulation. Accordingly, the per-layer overhead is dominated by

$$\mathcal{O}_{\text{SAA}} = \mathcal{O}(d_\phi(2d + d_h)) + \mathcal{O}(d_\phi^2) + \mathcal{O}(rd_\phi) + \mathcal{O}(mr). \quad (33)$$

Since both the bottleneck dimension  $r$  and the control dimension  $d_\phi$  are much smaller than the backbone width, the overhead introduced by SAA remains marginal compared with the linear sequence modeling cost of the Mamba backbone. Moreover, SAA preserves the linear-time scan structure of selective SSM, thereby maintaining the favorable linear-complexity property of Mamba while enabling parameter-efficient downstream adaptation.

## B More experimental results

### B.1 Training detail

All experiments, including classification, few-shot, and segmentation, follow the standard dataset splits as defined in the respective benchmarks, and results are averaged over multiple runs with different random seeds to ensure reproducibility.

We adopt downstream fine-tuning configurations in alignment with the pioneering work PointMamba[23], as in Table 5. For example, when fine-tuning on ModelNet40[45], the training process spans 300 epochs, using a cosine learning rate scheduler that starts at  $3e-4$ , with a 10-epoch warm-up period. The AdamW optimizer is employed. All experiments are conducted on a single GeForce RTX 5090 using PyTorch version 2.7.1+cu128.

Table 5: Implementation details for various downstream tasks.

Configuration	Classification		Few-shot	Segmentation
	ModelNet40	ScanObjectNN	ModelNet40	ShapeNetPart
Optimizer	AdamW	AdamW	AdamW	AdamW
Learning rate	3e-4	5e-4	3e-4	2e-4
Weight decay	5e-2	5e-2	5e-2	5e-2
Learning rate scheduler	cosine	cosine	cosine	cosine
Training epochs	300	300	150	300
Warm-up epochs	10	10	10	10
Batch size	32	32	32	16
$r$ in State-Aware Adapter	8	8	8	8
Softmax temperature $\tau$	1	1	1	1
Num. of encoder layers	12	12	12	12
Input points	1024	2048	1024	2048
Num. of patches	64	128	64	128
Patch size	32	32	32	32
Augmentation	Scale&Trans/Rotation	Scale&Trans	Scale&Trans	Scale&Trans

Table 6: Ablation study on Mantis based on Mamba3D[12], including sparse controller design, bottleneck dimension  $r$ , and scanning curves.

(a) The effect of different scanning curves.		(b) The effect of $r$ .			(c) The effect of controller design.		
Scanning curve	PB_T50_RS (%)	$r$	#TP (M)	PB_T50_RS (%)	Controller	#TP (M)	PB_T50_RS (%)
Random	91.74	8	0.84	93.48	Dense-MLP	0.95	92.71
Hilbert and Trans-Hilbert	<b>93.48</b>	16	1.00	93.50	Sigmoid Gate	0.84	92.88
Z-order and Trans-Z-order	92.86	32	1.32	<b>93.58</b>	Tanh Gate	0.84	92.97
Hilbert and Z-order	93.02	64	1.95	93.47	Hard-threshold	0.84	93.16
Trans-Hilbert and Trans-Z-order	93.21	72	2.12	93.41	Soft-threshold	0.84	<b>93.48</b>

## B.2 Additional ablation study

**Ablation study on different scanning curves.** We further study different scanning curves for constructing serialized point tokens, including Hilbert, Z-order, and their transposed variants. As shown in Table 6 (a), all structured scanning strategies consistently outperform random serialization on the hardest PB\_T50\_RS setting, indicating that geometry-aware traversal orders are important for stable state propagation in Mamba-based backbones. Moreover, since DSCD enforces consistency across two serialization branches, the scanning curves affect not only the sequence modeling quality within each branch, but also the complementarity between the two views. Among all candidates, the combination of Hilbert and Trans-Hilbert achieves the best performance, likely because it provides a favorable balance between locality preservation and cross-serialization diversity.

**Ablation study on bottleneck dimension  $r$ .** The SAA aims to reduce the number of trainable parameters during fine-tuning, and the bottleneck dimension  $r$  is introduced to balance adaptation efficiency and downstream performance. As shown in Table 6 (b), while increasing  $r$  moderately enlarges the adaptation capacity of SAA, the gain over  $r = 8$  remains marginal, suggesting that a small bottleneck is already sufficient to capture most of the useful task-specific modulation. Therefore, we adopt  $r = 8$  as the default setting, since it provides the most favorable trade-off between accuracy and parameter efficiency.

**Ablation study on controller design.** To examine whether the sparse proximal controller is necessary, we compare the proposed soft-thresholding controller with several dense or hard-selection alternatives under matched trainable parameters. As shown in Table 6 (c), replacing the soft-thresholding controller with Dense-MLP, Sigmoid Gate, Tanh Gate, or Hard-threshold consistently degrades performance. This indicates that the improvement of SAA lies not merely in low-rank dynamic parameterization, but also in sparse and magnitude-controlled perturbations induced by soft-thresholding. Therefore, the soft-thresholding controller provides a more stable and effective way to modulate frozen Mamba backbones.

Table 7: Ablation study on the internal design of SAA based on Mamba3D[12], including state fusion function and modulated state-space operators.

(a) Ablation on fusion function $\Phi(\cdot)$ .			(b) Ablation on modulated operators.		
Fusion function $\Phi(\cdot)$	#TP (M)	PB_T50_RS (%)	Modulated operators	#TP (M)	PB_T50_RS (%)
Addition	0.81	92.34	$A_t$ only	0.84	92.08
Concatenation	0.82	92.71	$B_t, C_t$ only	0.84	92.43
Gated Fusion	0.86	<u>93.21</u>	$\Delta_t$ only	0.84	92.31
Cross-attention Fusion	0.91	93.12	$A_t, \Delta_t$	0.84	92.67
Concat. + MLP	0.84	<b>93.48</b>	$B_t, C_t, \Delta_t$	0.84	92.96
			$A_t, B_t, C_t, \Delta_t$	0.84	<b>93.48</b>

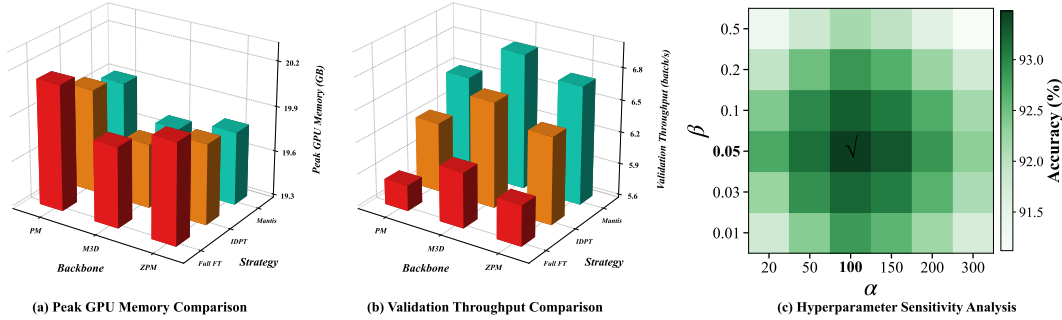


Figure 5: Comparison of computational efficiency and hyperparameter sensitivity on ScanObjectNN[36] (PB\_T50\_RS), where PM, M3D, and ZPM denote PointMamba[23], Mamba3D[12], and ZigzagPointMamba[7], respectively. Full FT, IDPT, and Mantis denote full fine-tuning, Instance-aware Dynamic Prompt Tuning [48], and our proposed method, respectively. (a) Peak GPU memory usage under different backbone and tuning strategy combinations. (b) Validation throughput under different backbone and tuning strategy combinations. (c) Sensitivity analysis of the DSCD hyperparameters  $\alpha$  and  $\beta$  on ScanObjectNN[36] based on Mamba3D[12].

**Ablation study on fusion function  $\Phi(\cdot)$ .** We further study different choices for the fusion function  $\Phi(\cdot)$  in SAA. As shown in Table 7 (a), simple addition or concatenation provides limited fusion capacity, while gated fusion and cross-attention fusion bring stronger results with more trainable parameters. In comparison, the proposed MLP-based fusion function achieves the best performance, suggesting that nonlinear fusion of the projected control features is beneficial for generating effective state-aware control signals.

**Ablation study on modulated operators.** We also examine which state-space operators should be modulated by SAA. As shown in Table 7 (b), modulating a single operator leads to inferior performance, indicating that adapting only one part of the selective SSM is insufficient. Jointly modulating  $B_t$ ,  $C_t$ , and  $\Delta_t$  further improves performance. The best result is achieved when  $A_t$ ,  $B_t$ ,  $C_t$ , and  $\Delta_t$  are modulated together. This supports the necessity of unified state-space operator modulation in SAA.

**Efficiency analysis.** We evaluate the computational efficiency of Mantis from the perspectives of peak GPU memory and validation throughput. As shown in Figure 5 (a), Mantis introduces only marginal memory overhead compared with Full FT and IDPT[48] across different Mamba-based backbones, indicating that the proposed state-aware adaptation remains lightweight in terms of GPU memory consumption. Figure 5 (b) further compares the validation throughput under the same backbone and tuning settings. Mantis maintains competitive throughput with stronger downstream performance, suggesting that SAA preserves the efficiency advantage of Mamba-based backbones.

**Hyperparameter sensitivity analysis.** We analyze the sensitivity of DSCD to the loss weights  $\alpha$  and  $\beta$ . As shown in Figure 5 (c), Mantis is relatively stable across a broad range of hyperparameter choices, indicating that the effectiveness of DSCD is not restricted to a single carefully tuned setting. The best performance is achieved around  $\alpha = 100$  and  $\beta = 0.05$ , which are therefore adopted as the default hyperparameters in our experiments.

Table 8: Comparison results of large-scale indoor scene semantic segmentation on S3DIS Area 5[2]. The input modality, mean class accuracy (mAcc), and mean IoU (mIoU) are reported. \* denotes results reproduced from the public source code.

Method	#TP (M)	Input	mAcc (%)	mIoU (%)
PointNet[28]	3.6	xyz+rgb	49.0	41.1
PointCNN[22]	3.6	xyz+rgb	63.9	57.3
PointNet++[29]	1.0	xyz+rgb	67.1	53.5
Point-BERT[47]	27.0	xyz	69.7	60.5
Point-MAE[27]	27.0	xyz	69.9	60.8
Transformer[38]	27.0	xyz	68.6	60.0
ReCon <sup>*</sup> [30]	27.0	xyz	69.3	60.4
+ IDPT <sup>*</sup> [48]	5.6	xyz	64.8 (- 4.5)	52.6 (- 7.8)
+ PMA <sup>*</sup> [50]	5.8	xyz	68.1 (- 1.2)	58.9 (- 1.5)
Mamba3D <sup>*</sup> [12]	21.9	xyz	68.2	58.4
+ PMA <sup>*</sup> [50]	6.0	xyz	64.9 (- 3.3)	54.6 (- 3.8)
+ Mantis	7.2	xyz	67.9 (- 0.3)	57.1 (- 1.3)

### B.3 Large-scale indoor scene semantic segmentation

We evaluate Mantis on S3DIS Area 5[2] to examine its scalability to large-scale indoor scene understanding. For a fair comparison, we reproduce baselines without reported results under the same S3DIS Area 5 protocol. The training settings are aligned as closely as possible. As shown in Table 8, semantic segmentation requires a relatively large task-specific head, resulting in comparable trainable parameter counts across PEFT methods. Under this setting, Mantis achieves the closest performance to full fine-tuning among the efficient variants on the Mamba3D backbone, while IDPT and PMA suffer from more noticeable degradation. This suggests that the proposed state-aware adaptation can better preserve the dense prediction ability of frozen Mamba backbones. These results further support the effectiveness of Mantis on large-scale scene-level understanding.

### B.4 Detailed results for classification and segmentation

To provide a more fine-grained evaluation, we report per-category results for both object classification and part segmentation. Table 9 reports category-wise IoU on ShapeNetPart[46], while Table 10 presents class-wise classification accuracy on ScanObjectNN[36] (PB\_T50\_RS). The results show that the improvement of Mantis is not concentrated on a few categories, but is generally consistent across different object and part classes.

For part segmentation, Mantis maintains competitive instance-level mIoU and improves class-level mIoU across all three Mamba-based backbones. The gains on categories such as “Bag”, “Cap”, “Knife”, “Lamp”, “Mug”, and “Rocket” suggest that Mantis is effective in preserving fine-grained local geometric structures under parameter-efficient adaptation. For object classification, Mantis consistently improves both mAcc and OA over the corresponding full fine-tuning baselines, with clear gains on challenging categories such as “Bag”, “Box”, “Desk”, “Bed”, “Pillow”, and “Sink”. These categories often exhibit larger intra-class variation or stronger geometric ambiguity, indicating that state-aware adaptation and cross-serialization consistency help improve robustness under noisy and order-sensitive real-world point cloud inputs.

### B.5 Part segmentation visualization

In Figure 7, 8, and 9, we visualize our Mantis part segmentation results on the Mamba3D[12] baseline. We present all 16 ShapeNetPart[46] categories from four different viewpoints. Mantis accurately segments large, well-defined parts such as airplane wings and chair seats, while also capturing small or complex parts like guitar strings and mug handles. The four-view visualizations demonstrate robustness to different camera angles and occlusions, maintaining consistent part predictions. Even fine-grained structures are well-preserved, highlighting effective feature aggregation and state-aware adaptation. Color-coded part labels clearly separate adjacent parts, reducing ambiguity. Despite achieving these visual results, Mantis introduces only a small number of trainable parameters,

Table 9: Per-category part segmentation results on ShapeNetPart[46]. We report instance-level mIoU, class-level mIoU, and category-wise IoU (%).

Methods	Inst.	Cls.	Air.	Bag	Cup	Car	Chair	Ear.	Guitar	Knife	Lamp	Laptop	Motor.	Mug	Pistol	Rocket	Skate.	Table
<i>Full Fine-tuning</i>																		
PointMamba	85.3	82.6	83.3	83.5	86.6	79.0	90.0	77.5	90.7	86.1	83.9	94.6	72.8	93.4	83.5	60.4	74.7	81.6
Mamba3D	85.6	83.6	83.7	84.3	87.5	78.5	91.2	80.6	91.2	87.5	87.1	95.6	74.2	94.2	83.7	68.6	74.6	83.3
ZigzagPointMamba	85.8	84.2	84.3	84.7	87.9	78.5	91.2	80.6	91.2	87.5	87.1	95.6	74.2	94.2	83.7	68.6	74.6	83.3
<i>Parameter-Efficient Fine-tuning</i>																		
PointMamba + Mantis	85.1	82.9	83.0	84.0	87.0	78.6	89.8	78.5	90.6	86.5	84.9	94.8	73.3	93.6	83.7	62.2	74.8	81.1
Mamba3D + Mantis	86.1	84.1	83.9	84.7	87.9	78.2	91.2	80.4	91.0	87.5	87.1	95.6	74.2	94.2	83.7	68.1	74.6	83.1
ZigzagPointMamba + Mantis	85.9	84.5	84.5	84.9	88.1	78.3	91.4	81.1	91.3	87.8	87.7	95.8	74.5	94.4	83.9	70.1	74.6	83.6

Table 10: Per-class classification accuracy on ScanObjectNN[36] (PB\_T50\_RS). We report mean class accuracy (mAcc), overall accuracy (OA), and class-wise accuracy (%).

Methods	mAcc	OA	Bag	Bin	Box	Cab.	Chair	Desk	Display	Door	Shelf	Table	Bed	Pillow	Sink	Sofa	Toilet
<i>Full Fine-tuning</i>																	
PointMamba	87.6	89.3	81.0	89.2	75.2	89.1	92.8	85.5	89.0	92.4	88.9	87.6	86.8	88.9	87.5	92.0	87.7
Mamba3D	90.2	92.1	83.8	92.0	78.2	91.6	95.5	88.2	91.4	95.2	91.6	90.2	89.4	91.3	89.8	94.6	90.2
ZigzagPointMamba	86.9	88.7	79.9	88.9	73.6	88.5	92.3	84.5	88.7	92.3	88.5	86.8	86.2	88.2	86.6	91.5	87.0
<i>Parameter-Efficient Fine-tuning</i>																	
PointMamba + Mantis	88.3	90.0	82.5	90.0	77.0	89.6	92.9	86.8	89.4	92.6	89.3	88.6	87.9	89.3	88.3	92.2	88.1
Mamba3D + Mantis	91.6	93.5	86.5	93.1	81.5	92.7	95.8	90.2	92.6	95.6	92.5	91.7	91.2	92.5	91.6	95.1	91.4
ZigzagPointMamba + Mantis	88.5	90.1	82.9	90.0	77.7	89.6	93.0	87.1	89.8	92.8	89.6	88.6	88.0	89.4	88.5	92.2	88.3

confirming its parameter-efficient design. Overall, these visualizations validate that Mantis provides accurate, robust, and efficient fine-grained part segmentation across diverse 3D objects.

## C Explanatory experiments and discussions

### C.1 Training dynamics and optimization stability

#### Observation: Token-Level Prompting Destabilizes Mamba Adaptation

Directly applying IDPT[48] to Mamba3D[12] leads to unstable training and inferior convergence, suggesting that token-level prompt tuning is poorly aligned with Mamba’s state-level sequence dynamics.

- **Mismatch:** IDPT is designed for Transformer-style token interactions, while Mamba relies on selective state-space dynamics and recurrent hidden-state propagation.
- **Mantis Design:** SAA adapts the state evolution directly, and DSCD regularizes predictions across different serialization orders.
- **Empirical Evidence:** Figure 6 illustrates that IDPT exhibits unstable training and slower convergence, whereas Mantis stabilizes training across challenging variants.

Mantis achieves smoother and more stable convergence, reaching performance comparable to or better than full fine-tuning with only about 5% of trainable parameters.

Although IDPT[48] is effective for Transformer-based point cloud backbones, directly applying it to Mamba3D[12] leads to unstable training dynamics and inferior convergence on downstream classification tasks. This observation is consistent with our motivation that token-level prompt tuning is not well aligned with the state-level sequence dynamics of Mamba. In contrast, Mantis introduces state-aware adaptation and dual-serialization consistency, which better match the selective state-space modeling mechanism. As a consequence, Mantis shows smoother and more stable convergence, especially on the challenging ScanObjectNN variants, and achieves final performance comparable to or better than full fine-tuning with only about 5% of trainable parameters.

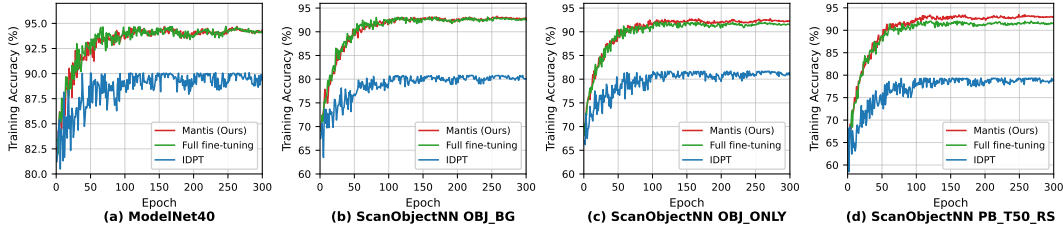


Figure 6: The classification accuracy curves of full fine-tuning, IDPT[48], and our Mantis with Mamba3D[12] on ModelNet40[45] and ScanObjectNN[36].

## C.2 Further analysis on PB\_T50\_RS

### Key Insight: Why Mantis Excels on PB\_T50\_RS

PB\_T50\_RS strongly exposes the order-sensitivity of frozen Mamba backbones in real-world point clouds. Mantis effectively addresses this through:

- **State-Aware Adapter (SAA):** Dynamically modulates state-space transitions to adapt hidden states under noisy or partially corrupted inputs.
- **Dual-Serialization Consistency Distillation (DSCD):** Aligns representations and predictions across different serialization orders, mitigating instability.
- **Empirical Evidence:** Table 11 shows that Mantis consistently reduces feature-level and prediction-level cross-serialization discrepancies, with the largest reduction on PB\_T50\_RS.

These effects stabilize downstream predictions and yield the largest gains on PB\_T50\_RS. This does not mean PB\_T50\_RS is easier. Rather, it simply highlights weaknesses of frozen Mamba backbones under noisy, order-sensitive inputs, where Mantis can be particularly effective.

An interesting phenomenon in Table 1 is that the advantage of Mantis becomes more pronounced on the most challenging PB\_T50\_RS split than on the relatively easier OBJ\_BG and OBJ\_ONLY variants. We conjecture that this trend is closely related to the order sensitivity of Mamba-style sequence modeling on point clouds. Since point clouds are inherently unordered, the hidden-state propagation of a serialized selective SSM depends on the adopted traversal order. When the input is relatively clean and structurally regular, such order sensitivity may have only a limited effect. However, under more challenging real-world scans with stronger clutter, occlusion, and geometric corruption, different valid serializations are more likely to induce larger discrepancies in state propagation and feature aggregation. In this regime, the robustness benefit of Mantis becomes more evident.

To verify this explanation, we further measure the feature-level and prediction-level cross-serialization discrepancies on different ScanObjectNN variants using the same formulations as the consistency terms in Sec. 3.4. Lower values indicate stronger consistency across different serialization views.

Table 11: Cross-serialization discrepancy on different ScanObjectNN[36] variants.

Methods	OBJ_BG		OBJ_ONLY		PB_T50_RS	
	Feat. Disc.	Pred. Disc.	Feat. Disc.	Pred. Disc.	Feat. Disc.	Pred. Disc.
Mamba3D + Full Fine-tuning	0.148	0.031	0.136	0.027	0.221	0.054
Mamba3D + Mantis	0.109 (↓ 26.4%)	0.019 (↓ 38.7%)	0.101 (↓ 25.7%)	0.017 (↓ 37.0%)	0.128 (↓ 42.1%)	0.024 (↓ 55.6%)

As shown in Table 11, the baseline model exhibits the largest feature-level and prediction-level discrepancy on PB\_T50\_RS among the three ScanObjectNN variants, confirming that harder real-world point clouds indeed amplify serialization sensitivity. In contrast, Mantis consistently reduces both discrepancies across all three variants, with the most substantial reduction observed on PB\_T50\_RS. This observation supports our hypothesis that the stronger performance of Mantis on the hardest split mainly stems from improved robustness to serialization-induced instability.

From a modeling perspective, this behavior can be understood from the complementary effects of the two components in Mantis. On the one hand, SAA dynamically modulates the state-space dynamics conditioned on the current input and latent state, enabling the frozen Mamba backbone to adapt its state evolution more flexibly under noisy and partially corrupted observations. On the other hand, DSCD explicitly regularizes the two serialization branches by aligning their feature representations and predictive distributions, thereby mitigating the instability caused by different traversal orders. When real-world perturbation and serialization ambiguity become more severe, the advantage of Mantis becomes particularly evident.

Importantly, this phenomenon should not be interpreted as PB\_T50\_RS being easier. Rather, it indicates that PB\_T50\_RS more strongly exposes the weakness of frozen Mamba backbones under noisy and order-sensitive inputs, thus creating a setting in which our robustness-oriented design is especially effective.

### C.3 Discussion on the scope of Mamba-native adaptation

#### Clarification: Scope of Mamba-Native Adaptation

While PMA[50] introduces Mamba modules for feature fusion on Transformer backbones, it does not adapt the frozen Mamba backbone itself. In contrast, Mantis directly modulates state-space operators ( $\mathbf{A}_t, \mathbf{B}_t, \mathbf{C}_t, \mathbf{\Delta}_t$ ) inside frozen Mamba backbones, performing true state-level adaptation.

- **PMA:** Acts as an auxiliary adapter on intermediate features; evaluated on Transformer-style PFMs; cannot fully exploit Mamba backbone dynamics.
- **Mantis:** Targets the backbone itself, aligning PEFT with Mamba’s state-level dynamics, achieving stronger performance on frozen Mamba backbones.
- **Implication:** Designing Mamba-native PEFT requires adaptation mechanisms matched to state-space modeling, rather than reusing Mamba modules for PEFT.

Overall, Mantis is not about using Mamba as an external module, but about serving Mamba backbones through state-level adaptation.

We further clarify the scope of “Mamba-native” adaptation in this work. PMA[50] is an important 3D PEFT baseline that introduces Mamba into point cloud adaptation. However, its design motivation and adaptation target are different from ours. PMA is motivated by the observation that intermediate features of a frozen pre-trained model contain complementary information that is often discarded by conventional PEFT methods. Accordingly, PMA constructs an ordered sequence from intermediate-layer features and employs a Mamba adapter to fuse cross-layer semantics for downstream tasks. In its original formulation, the backbone is a frozen Transformer encoder, while Mamba is introduced as an orthogonal adapter for feature fusion. Notably, PMA focuses its evaluation on Transformer-style pre-trained backbones such as Point-BERT[47], Point-MAE[27], PointGPT[4], and ReCon[30], further reflecting its original scope as a feature-fusion adapter for existing PFMs rather than a method tailored to frozen Mamba backbone dynamics.

In contrast, Mantis targets frozen Mamba-based point cloud backbones themselves. Instead of inserting a Mamba module outside the backbone to aggregate intermediate features, Mantis adapts the selective state-space dynamics inside frozen Mamba backbones by modulating the state-space operators ( $\mathbf{A}_t, \mathbf{B}_t, \mathbf{C}_t, \mathbf{\Delta}_t$ ). Therefore, we consider “Mamba-native 3D PEFT” not as the first use of Mamba modules in 3D PEFT, but as a state-level adaptation framework specifically tailored to frozen Mamba-based point cloud backbones. This distinction can be summarized as follows: **PMA uses Mamba as an auxiliary adapter, whereas Mantis is designed for adapting Mamba backbones.**

This distinction also motivates our choice of PMA as a representative PEFT baseline. Since PMA is the closest existing 3D PEFT method involving Mamba modules, comparing with it allows us to examine whether a general Mamba-based adapter designed for feature fusion can be directly transferred to frozen Mamba backbones. The results show that such feature-level adapter fusion is not sufficient for Mamba-backbone adaptation. In contrast, Mantis consistently achieves stronger performance by directly modulating the internal state-space operators. This comparison highlights the necessity of designing PEFT mechanisms that are aligned with the state-level dynamics of Mamba, rather than only reusing Mamba as an external feature-fusion module.

## D Symbol table

To improve readability, Table 12 summarizes the main notations used throughout this paper, including symbols related to point cloud serialization, SAA, DSCD, and the theoretical analysis.

Table 12: Symbol table

Symbol	Meaning
$P \in \mathbb{R}^{M \times 3}$	Input point cloud with $M$ points.
$p \in \mathbb{R}^{n \times 3}$	Sampled key points after Farthest Point Sampling (FPS).
$p_h, p_{h'}$	Two valid serialized sequences of the same point cloud.
$K$	Number of nearest neighbors in each local patch.
$d, d_h$	Token feature dimension and hidden-state dimension.
$d_o$	Dimension of learnable order embedding.
$d_\phi$	Dimension of the shared control space in SAA.
$E_h^{(1)}, E_{h'}^{(2)}$	Token features under the two serialization orders.
$E^{(k)}$	Token features of branch $k$ ( $k \in \{1, 2\}$ ).
$o^{(k)}$	Learnable order embedding for branch $k$ .
$e^{(k)}$	Order-aware representation for branch $k$ .
$\mathcal{G}(\cdot)$	Lightweight transformation for order-aware representation.
$\tilde{Z}_l^{(k)}$	LN-projected feature in $l$ -th encoder block.
$X_l^{(k)}$	Intermediate feature fed into selective SSM.
$Z_l^{(k)}$	Output of $l$ -th encoder block.
$Z_0^{(k)}, Z_L^{(k)}$	Input/final feature of SAA-Mamba encoder.
$z^{(k)}$	Projected global embedding in DSCD ( $g_\varphi$ ).
$r$	Bottleneck dimension in SAA.
$m$	Dimension of modulated operator space.
$\alpha, \beta, \tau$	Feature/prediction loss weights and DSCD temperature.
$\mathbf{q}_t^{(k)}$	Driving vector before soft-thresholding.
$\boldsymbol{\lambda}_t^{(k)}$	Adaptive threshold vector.
$\mathbf{u}_t^{(k)}$	Sparse task-conditioned control signal.
$\delta_t^{(k)}$	Low-rank perturbation on operator space.
$h_t^{(k,0)}$	Hidden state from frozen backbone.
$\delta h_t^{(k)}$	Hidden-state deviation under SAA.
$\varepsilon_A, \varepsilon_B$	Perturbation bounds for controlled operators.
$H, X$	Upper bounds on hidden-state and input norms.
$\varphi(\cdot)$	Order modulation mapping.
$\Phi(\cdot)$	State fusion function in SAA.
$\mathcal{F}_{\text{SAA}}(\cdot)$	Selective SSM enhanced with SAA.
$g_\varphi(\cdot)$	Branch-shared projection head in DSCD.
$\mathbf{W}_{t,i}^{(k)}$	Selective transfer kernel from step $i$ to $t$ .
$\mathbf{W}_{t,i}^{(k,0)}$	Frozen backbone kernel without SAA.
$\Delta \mathbf{W}_{t,i}^{(k)}$	Perturbation of selective transfer kernel.
$\mathbf{U}, \mathbf{V}$	Low-rank modulation matrices.
$\mathcal{N}_h^{(1)}, \mathcal{N}_{h'}^{(2)}$	Local neighborhoods under two serialization branches.
$k$	Branch index for dual serialization.
$x_t^{(k)}, h_t^{(k)}, y_t^{(k)}$	Input, hidden state, and output at step $t$ .
$\ell^{(k)}, \pi^{(k)}$	Logits and softened prediction of branch $k$ .
$\mathbf{A}, \mathbf{B}, \mathbf{C}, \mathbf{\Delta}$	Continuous-time state-space operators.
$\bar{\mathbf{A}}, \bar{\mathbf{B}}$	Discretized SSM operators (ZOH).
$\hat{\mathbf{A}}_t^{(k)}, \hat{\mathbf{B}}_t^{(k)}$	Discretized controlled operators after SAA.
$\mathbf{A}_t^{(k)}, \mathbf{B}_t^{(k)}, \mathbf{C}_t^{(k)}, \mathbf{\Delta}_t^{(k)}$	Input-dependent selective SSM operators at step $t$ .
$\tilde{\mathbf{A}}_t^{(k)}, \tilde{\mathbf{B}}_t^{(k)}, \tilde{\mathbf{C}}_t^{(k)}, \tilde{\mathbf{\Delta}}_t^{(k)}$	Controlled operators after SAA modulation.
$W_x^\phi, W_h^\phi, W_e^\phi, W_{\text{drv}}^\psi, W_{\text{gt}}^\psi$	Learnable projection matrices in SAA.
$\mathcal{L}_{\text{task}}, \mathcal{L}_{\text{feat}}, \mathcal{L}_{\text{pred}}$	Task loss, feature consistency, and prediction consistency loss.

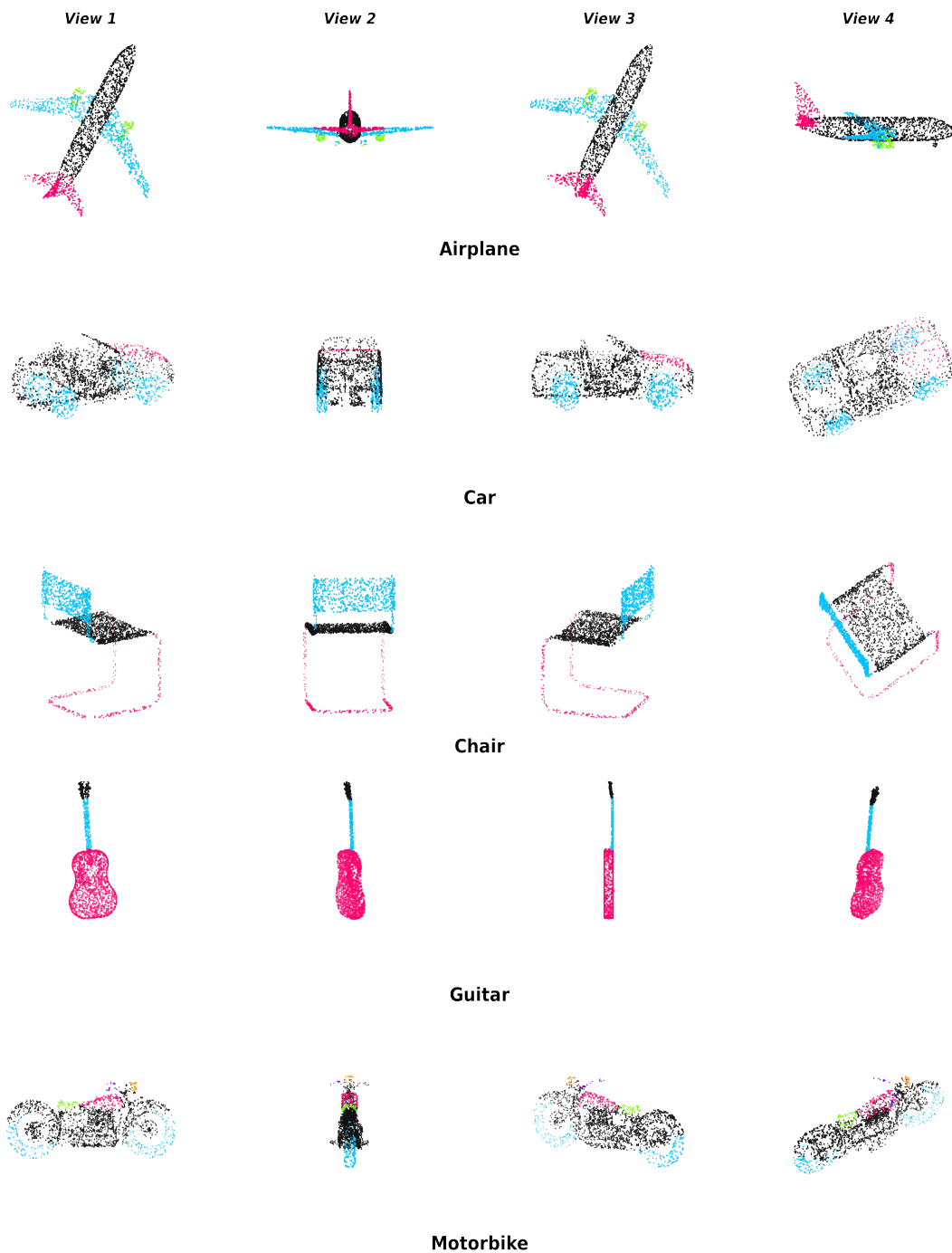


Figure 7: **Visualization results for part segmentation on ShapeNetPart[46].** Projected prediction images from Mantis are shown across four different viewpoints, including the categories “Airplane”, “Car”, “Chair”, “Guitar” and “Motorbike”.

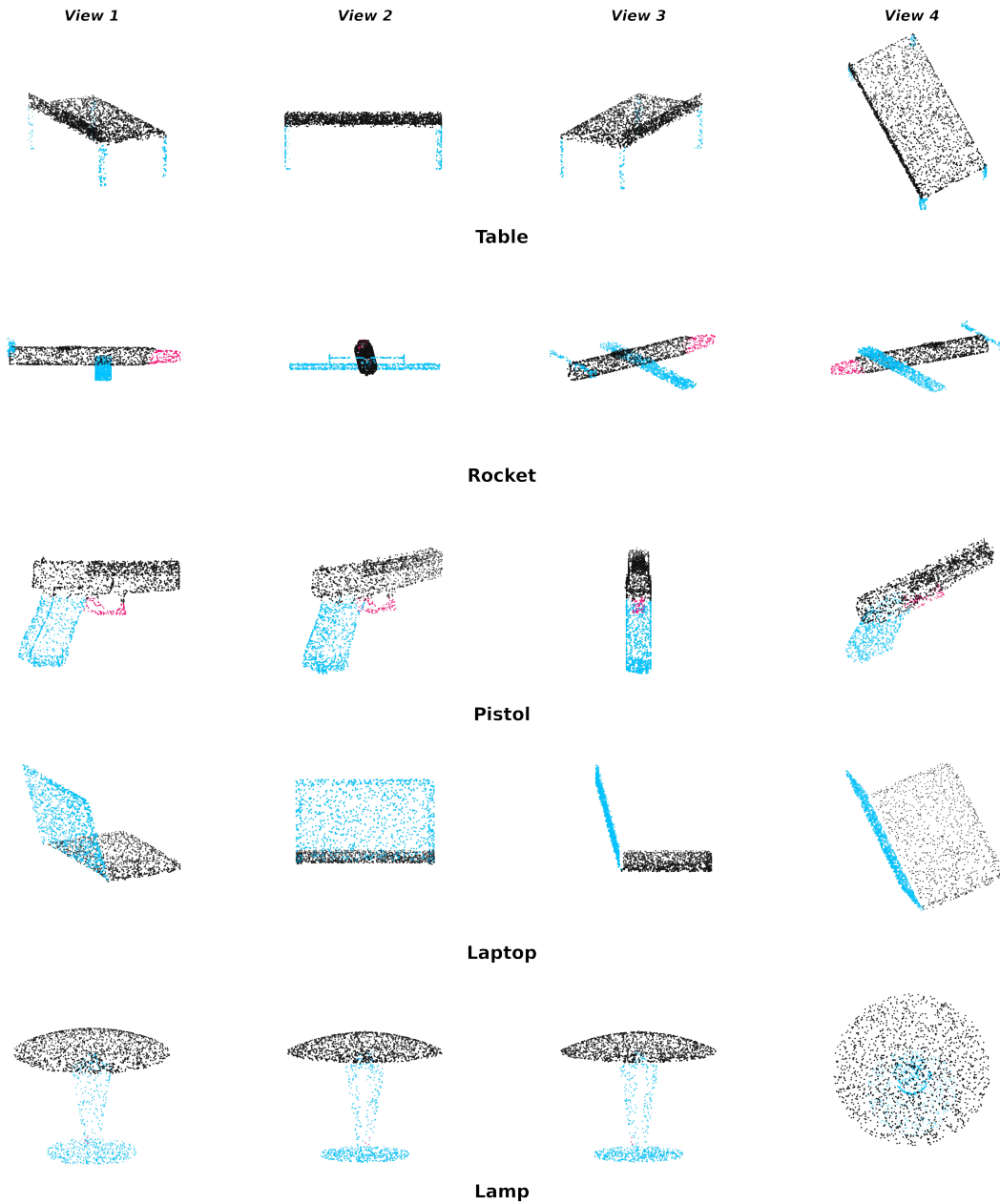


Figure 8: **Visualization results for part segmentation on ShapeNetPart[46]**. Projected prediction images from Mantis are shown across four different viewpoints, including the categories “Table”, “Rocket”, “Pistol”, “Laptop” and “Lamp”.

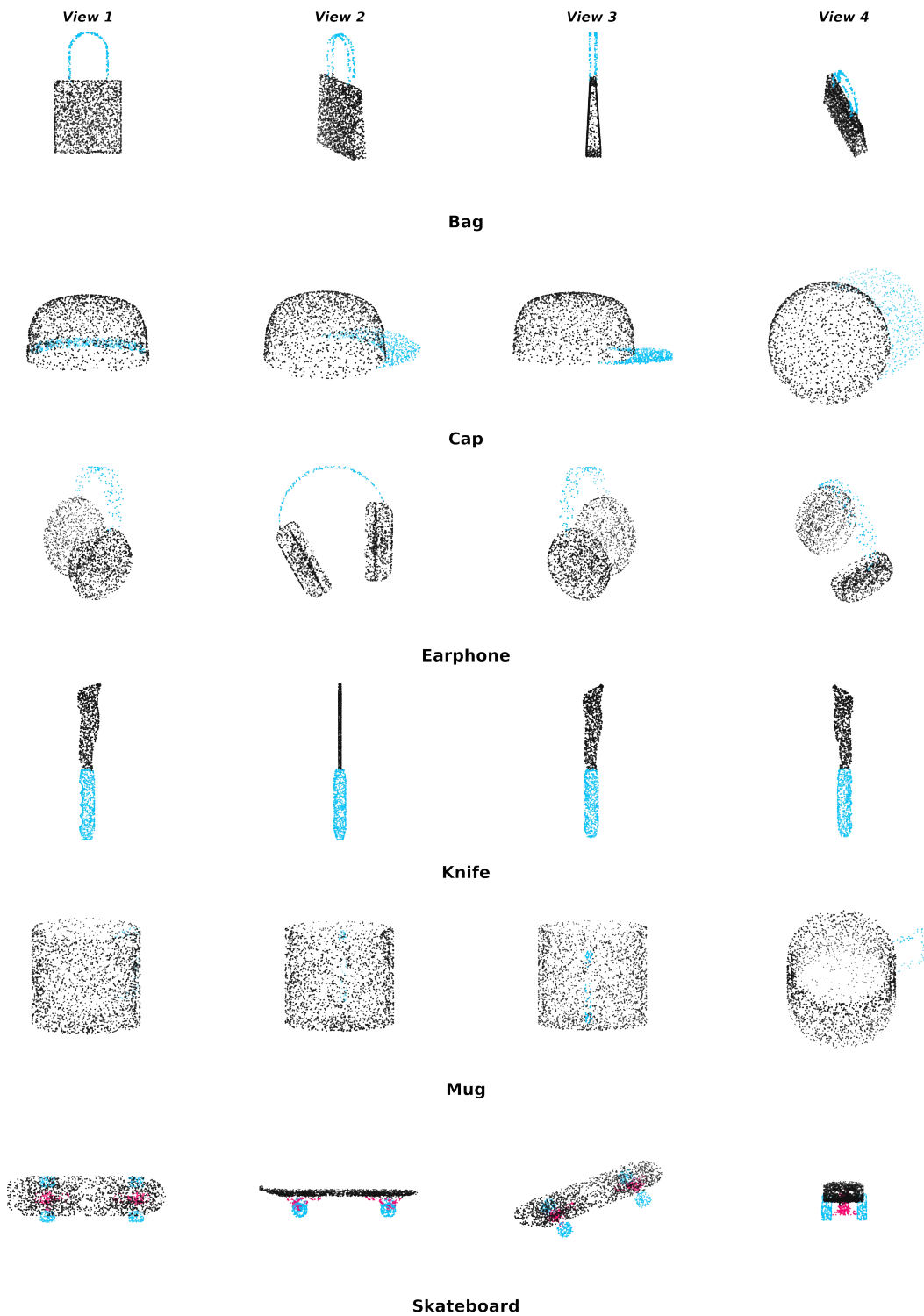


Figure 9: **Visualization results for part segmentation on ShapeNetPart[46].** Projected prediction images from Mantis are shown across four different viewpoints, including the categories “Bag”, “Cap”, “Earphone”, “Knife”, “Mug” and “Skateboard”.

## NeurIPS Paper Checklist

### 1. Claims

Question: Do the main claims made in the abstract and introduction accurately reflect the paper’s contributions and scope?

Answer: [Yes]

Justification: The abstract and introduction accurately summarize the main contributions of Mantis, including SAA and DSCD, which are supported by the methods and experimental results in Sections 3–4 and the appendix.

Guidelines:

- The answer [N/A] means that the abstract and introduction do not include the claims made in the paper.
- The abstract and/or introduction should clearly state the claims made, including the contributions made in the paper and important assumptions and limitations. A [No] or [N/A] answer to this question will not be perceived well by the reviewers.
- The claims made should match theoretical and experimental results, and reflect how much the results can be expected to generalize to other settings.
- It is fine to include aspirational goals as motivation as long as it is clear that these goals are not attained by the paper.

### 2. Limitations

Question: Does the paper discuss the limitations of the work performed by the authors?

Answer: [Yes]

Justification: Section 5 explicitly discusses limitations, including manually chosen configurations and the focus on single-modal point clouds, acknowledging areas for future improvement.

Guidelines:

- The answer [N/A] means that the paper has no limitation while the answer [No] means that the paper has limitations, but those are not discussed in the paper.
- The authors are encouraged to create a separate “Limitations” section in their paper.
- The paper should point out any strong assumptions and how robust the results are to violations of these assumptions (e.g., independence assumptions, noiseless settings, model well-specification, asymptotic approximations only holding locally). The authors should reflect on how these assumptions might be violated in practice and what the implications would be.
- The authors should reflect on the scope of the claims made, e.g., if the approach was only tested on a few datasets or with a few runs. In general, empirical results often depend on implicit assumptions, which should be articulated.
- The authors should reflect on the factors that influence the performance of the approach. For example, a facial recognition algorithm may perform poorly when image resolution is low or images are taken in low lighting. Or a speech-to-text system might not be used reliably to provide closed captions for online lectures because it fails to handle technical jargon.
- The authors should discuss the computational efficiency of the proposed algorithms and how they scale with dataset size.
- If applicable, the authors should discuss possible limitations of their approach to address problems of privacy and fairness.
- While the authors might fear that complete honesty about limitations might be used by reviewers as grounds for rejection, a worse outcome might be that reviewers discover limitations that aren’t acknowledged in the paper. The authors should use their best judgment and recognize that individual actions in favor of transparency play an important role in developing norms that preserve the integrity of the community. Reviewers will be specifically instructed to not penalize honesty concerning limitations.

### 3. Theory assumptions and proofs

Question: For each theoretical result, does the paper provide the full set of assumptions and a complete (and correct) proof?

Answer: [Yes]

Justification: Appendix A provides the assumptions and derivations for the theoretical analyses, including the selective transfer kernel, sparse low-rank SAA perturbation, bounded hidden-state deviation, and parameter/complexity analysis.

Guidelines:

- The answer [N/A] means that the paper does not include theoretical results.
- All the theorems, formulas, and proofs in the paper should be numbered and cross-referenced.
- All assumptions should be clearly stated or referenced in the statement of any theorems.
- The proofs can either appear in the main paper or the supplemental material, but if they appear in the supplemental material, the authors are encouraged to provide a short proof sketch to provide intuition.
- Inversely, any informal proof provided in the core of the paper should be complemented by formal proofs provided in appendix or supplemental material.
- Theorems and Lemmas that the proof relies upon should be properly referenced.

#### 4. Experimental result reproducibility

Question: Does the paper fully disclose all the information needed to reproduce the main experimental results of the paper to the extent that it affects the main claims and/or conclusions of the paper (regardless of whether the code and data are provided or not)?

Answer: [Yes]

Justification: The paper provides the information needed to reproduce the main experiments, including the method details, datasets, evaluation protocols, and training configurations in Sections 3–4 and Appendix B.1.

Guidelines:

- The answer [N/A] means that the paper does not include experiments.
- If the paper includes experiments, a [No] answer to this question will not be perceived well by the reviewers: Making the paper reproducible is important, regardless of whether the code and data are provided or not.
- If the contribution is a dataset and/or model, the authors should describe the steps taken to make their results reproducible or verifiable.
- Depending on the contribution, reproducibility can be accomplished in various ways. For example, if the contribution is a novel architecture, describing the architecture fully might suffice, or if the contribution is a specific model and empirical evaluation, it may be necessary to either make it possible for others to replicate the model with the same dataset, or provide access to the model. In general, releasing code and data is often one good way to accomplish this, but reproducibility can also be provided via detailed instructions for how to replicate the results, access to a hosted model (e.g., in the case of a large language model), releasing of a model checkpoint, or other means that are appropriate to the research performed.
- While NeurIPS does not require releasing code, the conference does require all submissions to provide some reasonable avenue for reproducibility, which may depend on the nature of the contribution. For example
  - (a) If the contribution is primarily a new algorithm, the paper should make it clear how to reproduce that algorithm.
  - (b) If the contribution is primarily a new model architecture, the paper should describe the architecture clearly and fully.
  - (c) If the contribution is a new model (e.g., a large language model), then there should either be a way to access this model for reproducing the results or a way to reproduce the model (e.g., with an open-source dataset or instructions for how to construct the dataset).

- (d) We recognize that reproducibility may be tricky in some cases, in which case authors are welcome to describe the particular way they provide for reproducibility. In the case of closed-source models, it may be that access to the model is limited in some way (e.g., to registered users), but it should be possible for other researchers to have some path to reproducing or verifying the results.

## 5. Open access to data and code

Question: Does the paper provide open access to the data and code, with sufficient instructions to faithfully reproduce the main experimental results, as described in supplemental material?

Answer: [Yes]

Justification: The code is provided in the supplementary material with instructions for environment setup, data preparation, and commands to reproduce the main experimental results.

Guidelines:

- The answer [N/A] means that paper does not include experiments requiring code.
- Please see the NeurIPS code and data submission guidelines (<https://neurips.cc/public/guides/CodeSubmissionPolicy>) for more details.
- While we encourage the release of code and data, we understand that this might not be possible, so [No] is an acceptable answer. Papers cannot be rejected simply for not including code, unless this is central to the contribution (e.g., for a new open-source benchmark).
- The instructions should contain the exact command and environment needed to run to reproduce the results. See the NeurIPS code and data submission guidelines (<https://neurips.cc/public/guides/CodeSubmissionPolicy>) for more details.
- The authors should provide instructions on data access and preparation, including how to access the raw data, preprocessed data, intermediate data, and generated data, etc.
- The authors should provide scripts to reproduce all experimental results for the new proposed method and baselines. If only a subset of experiments are reproducible, they should state which ones are omitted from the script and why.
- At submission time, to preserve anonymity, the authors should release anonymized versions (if applicable).
- Providing as much information as possible in supplemental material (appended to the paper) is recommended, but including URLs to data and code is permitted.

## 6. Experimental setting/details

Question: Does the paper specify all the training and test details (e.g., data splits, hyperparameters, how they were chosen, type of optimizer) necessary to understand the results?

Answer: [Yes]

Justification: Appendix B.1 specifies all training and test details, including datasets, data splits, hyperparameters, optimizer settings, and augmentation, sufficient to reproduce the results.

Guidelines:

- The answer [N/A] means that the paper does not include experiments.
- The experimental setting should be presented in the core of the paper to a level of detail that is necessary to appreciate the results and make sense of them.
- The full details can be provided either with the code, in appendix, or as supplemental material.

## 7. Experiment statistical significance

Question: Does the paper report error bars suitably and correctly defined or other appropriate information about the statistical significance of the experiments?

Answer: [Yes]

Justification: Few-shot experiments (Table 2) report mean  $\pm$  standard deviation over 10 runs; other experiments follow standard splits and repeated runs as detailed in Appendix B.1.

Guidelines:

- The answer [N/A] means that the paper does not include experiments.
- The authors should answer [Yes] if the results are accompanied by error bars, confidence intervals, or statistical significance tests, at least for the experiments that support the main claims of the paper.
- The factors of variability that the error bars are capturing should be clearly stated (for example, train/test split, initialization, random drawing of some parameter, or overall run with given experimental conditions).
- The method for calculating the error bars should be explained (closed form formula, call to a library function, bootstrap, etc.)
- The assumptions made should be given (e.g., Normally distributed errors).
- It should be clear whether the error bar is the standard deviation or the standard error of the mean.
- It is OK to report 1-sigma error bars, but one should state it. The authors should preferably report a 2-sigma error bar than state that they have a 96% CI, if the hypothesis of Normality of errors is not verified.
- For asymmetric distributions, the authors should be careful not to show in tables or figures symmetric error bars that would yield results that are out of range (e.g., negative error rates).
- If error bars are reported in tables or plots, the authors should explain in the text how they were calculated and reference the corresponding figures or tables in the text.

#### 8. Experiments compute resources

Question: For each experiment, does the paper provide sufficient information on the computer resources (type of compute workers, memory, time of execution) needed to reproduce the experiments?

Answer: [Yes]

Justification: As detailed in Appendix B.1, all experiments were conducted on a single GeForce RTX 5090 GPU with PyTorch 2.7.1+cu128, and Figure 5 reports the peak GPU memory usage and validation throughput.

Guidelines:

- The answer [N/A] means that the paper does not include experiments.
- The paper should indicate the type of compute workers CPU or GPU, internal cluster, or cloud provider, including relevant memory and storage.
- The paper should provide the amount of compute required for each of the individual experimental runs as well as estimate the total compute.
- The paper should disclose whether the full research project required more compute than the experiments reported in the paper (e.g., preliminary or failed experiments that didn't make it into the paper).

#### 9. Code of ethics

Question: Does the research conducted in the paper conform, in every respect, with the NeurIPS Code of Ethics [https://neurips.cc/public/EthicsGuidelines?](https://neurips.cc/public/EthicsGuidelines)

Answer: [Yes]

Justification: The research complies with the NeurIPS Code of Ethics, as it does not involve human subjects, sensitive data, or high-risk model/data release.

Guidelines:

- The answer [N/A] means that the authors have not reviewed the NeurIPS Code of Ethics.
- If the authors answer [No], they should explain the special circumstances that require a deviation from the Code of Ethics.
- The authors should make sure to preserve anonymity (e.g., if there is a special consideration due to laws or regulations in their jurisdiction).

#### 10. Broader impacts

Question: Does the paper discuss both potential positive societal impacts and negative societal impacts of the work performed?

Answer: [N/A]

Justification: This work focuses on parameter-efficient adaptation for 3D point cloud models and does not have a direct path to negative societal applications. The research is foundational in nature and is not tied to any specific deployment scenario that would require an impact discussion.

Guidelines:

- The answer [N/A] means that there is no societal impact of the work performed.
- If the authors answer [N/A] or [No], they should explain why their work has no societal impact or why the paper does not address societal impact.
- Examples of negative societal impacts include potential malicious or unintended uses (e.g., disinformation, generating fake profiles, surveillance), fairness considerations (e.g., deployment of technologies that could make decisions that unfairly impact specific groups), privacy considerations, and security considerations.
- The conference expects that many papers will be foundational research and not tied to particular applications, let alone deployments. However, if there is a direct path to any negative applications, the authors should point it out. For example, it is legitimate to point out that an improvement in the quality of generative models could be used to generate Deepfakes for disinformation. On the other hand, it is not needed to point out that a generic algorithm for optimizing neural networks could enable people to train models that generate Deepfakes faster.
- The authors should consider possible harms that could arise when the technology is being used as intended and functioning correctly, harms that could arise when the technology is being used as intended but gives incorrect results, and harms following from (intentional or unintentional) misuse of the technology.
- If there are negative societal impacts, the authors could also discuss possible mitigation strategies (e.g., gated release of models, providing defenses in addition to attacks, mechanisms for monitoring misuse, mechanisms to monitor how a system learns from feedback over time, improving the efficiency and accessibility of ML).

## 11. Safeguards

Question: Does the paper describe safeguards that have been put in place for responsible release of data or models that have a high risk for misuse (e.g., pre-trained language models, image generators, or scraped datasets)?

Answer: [N/A]

Justification: The paper does not release high-risk models or datasets; no special safeguards are required for responsible use.

Guidelines:

- The answer [N/A] means that the paper poses no such risks.
- Released models that have a high risk for misuse or dual-use should be released with necessary safeguards to allow for controlled use of the model, for example by requiring that users adhere to usage guidelines or restrictions to access the model or implementing safety filters.
- Datasets that have been scraped from the Internet could pose safety risks. The authors should describe how they avoided releasing unsafe images.
- We recognize that providing effective safeguards is challenging, and many papers do not require this, but we encourage authors to take this into account and make a best faith effort.

## 12. Licenses for existing assets

Question: Are the creators or original owners of assets (e.g., code, data, models), used in the paper, properly credited and are the license and terms of use explicitly mentioned and properly respected?

Answer: [Yes]

Justification: All datasets and pre-trained models used (ScanObjectNN, ModelNet40, ShapeNetPart, PointMamba, Mamba3D) are properly credited to the original creators, and their usage respects the intended terms as described in the original papers.

Guidelines:

- The answer [N/A] means that the paper does not use existing assets.
- The authors should cite the original paper that produced the code package or dataset.
- The authors should state which version of the asset is used and, if possible, include a URL.
- The name of the license (e.g., CC-BY 4.0) should be included for each asset.
- For scraped data from a particular source (e.g., website), the copyright and terms of service of that source should be provided.
- If assets are released, the license, copyright information, and terms of use in the package should be provided. For popular datasets, [paperswithcode.com/datasets](https://paperswithcode.com/datasets) has curated licenses for some datasets. Their licensing guide can help determine the license of a dataset.
- For existing datasets that are re-packaged, both the original license and the license of the derived asset (if it has changed) should be provided.
- If this information is not available online, the authors are encouraged to reach out to the asset's creators.

### 13. **New assets**

Question: Are new assets introduced in the paper well documented and is the documentation provided alongside the assets?

Answer: [Yes]

Justification: The paper releases all configuration files used in the experiments, along with documentation on how to use them to reproduce the results.

Guidelines:

- The answer [N/A] means that the paper does not release new assets.
- Researchers should communicate the details of the dataset/code/model as part of their submissions via structured templates. This includes details about training, license, limitations, etc.
- The paper should discuss whether and how consent was obtained from people whose asset is used.
- At submission time, remember to anonymize your assets (if applicable). You can either create an anonymized URL or include an anonymized zip file.

### 14. **Crowdsourcing and research with human subjects**

Question: For crowdsourcing experiments and research with human subjects, does the paper include the full text of instructions given to participants and screenshots, if applicable, as well as details about compensation (if any)?

Answer: [N/A]

Justification: The paper does not involve crowdsourcing experiments or research with human subjects.

Guidelines:

- The answer [N/A] means that the paper does not involve crowdsourcing nor research with human subjects.
- Including this information in the supplemental material is fine, but if the main contribution of the paper involves human subjects, then as much detail as possible should be included in the main paper.
- According to the NeurIPS Code of Ethics, workers involved in data collection, curation, or other labor should be paid at least the minimum wage in the country of the data collector.

### 15. **Institutional review board (IRB) approvals or equivalent for research with human subjects**

Question: Does the paper describe potential risks incurred by study participants, whether such risks were disclosed to the subjects, and whether Institutional Review Board (IRB) approvals (or an equivalent approval/review based on the requirements of your country or institution) were obtained?

Answer: [N/A]

Justification: The paper does not involve research with human subjects or require IRB approval.

Guidelines:

- The answer [N/A] means that the paper does not involve crowdsourcing nor research with human subjects.
- Depending on the country in which research is conducted, IRB approval (or equivalent) may be required for any human subjects research. If you obtained IRB approval, you should clearly state this in the paper.
- We recognize that the procedures for this may vary significantly between institutions and locations, and we expect authors to adhere to the NeurIPS Code of Ethics and the guidelines for their institution.
- For initial submissions, do not include any information that would break anonymity (if applicable), such as the institution conducting the review.

#### 16. Declaration of LLM usage

Question: Does the paper describe the usage of LLMs if it is an important, original, or non-standard component of the core methods in this research? Note that if the LLM is used only for writing, editing, or formatting purposes and does *not* impact the core methodology, scientific rigor, or originality of the research, declaration is not required.

Answer: [N/A]

Justification: This work does not use LLMs as part of the core methods; any language model usage was not relevant to the research methodology.

Guidelines:

- The answer [N/A] means that the core method development in this research does not involve LLMs as any important, original, or non-standard components.
- Please refer to our LLM policy in the NeurIPS handbook for what should or should not be described.